Acta Pharmaceutica Sinica B 2025;15(9):4711−4729

Chinese Pharmaceutical Association
Institute of Materia Medica, Chinese Academy of Medical Sciences

Acta Pharmaceutica Sinica B

www.elsevier.com/locate/apsb
www.sciencedirect.com

ORIGINAL ARTICLE

Evidence that metformin promotes fibrosis resolution *via* activating alveolar epithelial stem cells and FGFR2b signaling

Yuqing Lv[a,b,c,d], Yanxia Zhang[c], Xueli Guo[c], Baiqi He[c], Haibo Xu[c], Ming Xu[c], Lihui Zou[d], Handeng Lyu[c], Jin Wu[c,d], Pingping Zeng[d], Saverio Bellusci[a,e], Xuru Jin[a], Chengshui Chen[a], Young-Chang Cho[b,*], Xiaokun Li[d,*], Jin-San Zhang[a,c,d,f,*]

[a]*The Quzhou Affiliated Hospital of Wenzhou Medical University (Quzhou People's Hospital), Quzhou 324000, China*
[b]*College of Pharmacy and Research Institute of Pharmaceutical Sciences, Chonnam National University, Gwangju 61186, Republic of Korea*
[c]*Medical Research Center, Zhejiang Key Laboratory of Interventional Pulmonology, the First Affiliated Hospital of Wenzhou Medical University, Wenzhou 325035, China*
[d]*International Collaborative Center on Growth Factor Research, School of Pharmaceutical Sciences, Wenzhou Medical University, Wenzhou 325035, China*
[e]*Cardio-Pulmonary Institute, Universities of Giessen and Marburg Lung Center, German Center for Lung Research (DZL), Justus Liebig University, Giessen 35392, Germany*
[f]*Zhejiang Key Laboratory of Intelligent Cancer Biomarker Discovery and Translation, First Affiliated Hospital, Wenzhou Medical University, Wenzhou 325035, China*

Received 4 February 2025; received in revised form 15 May 2025; accepted 23 May 2025

KEY WORDS

Alveolar stem cell;
Injury-activated alveolar progenitor;
Metformin;
Pulmonary fibrosis;
FGFR2b;

Abstract Idiopathic pulmonary fibrosis (IPF) is a progressive disease lacking effective therapy. Metformin, an antidiabetic medication, has shown promising therapeutic properties in preclinical fibrosis models; however, its precise cellular targets and associated mechanisms in fibrosis resolution remain incompletely defined. Most research on metformin's effects has focused on mesenchymal and inflammatory responses with limited attention to epithelial cells. In this study, we utilized *Sftpc* lineage-traced and *Fgfr2b* conditional knockout mice, along with BMP2/PPARγ and AMPK inhibitors, to explore metformin's impact on alveolar epithelial cells in a bleomycin-induced pulmonary fibrosis model and cell

*Corresponding authors.
E-mail addresses: yccho@jnu.ac.kr (Young-Chang Cho), Xiaokunli@wmu.edu.cn (Xiaokun Li), Zhang_JinSan@WMU.edu.cn (Jin-San Zhang).
Peer review under the responsibility of Chinese Pharmaceutical Association and Institute of Materia Medica, Chinese Academy of Medical Sciences.

https://doi.org/10.1016/j.apsb.2025.07.023
2211-3835 © 2025 The Authors. Published by Elsevier B.V. on behalf of Chinese Pharmaceutical Association and Institute of Materia Medica, Chinese Academy of Medical Sciences. This is an open access article under the CC BY-NC-ND license (http://creativecommons.org/licenses/by-nc-nd/4.0/).

AMPK;
Transgenic mice

culture. We found that metformin increased the proliferation and differentiation of alveolar type 2 (AT2) cells, particularly the recently identified injury-activated alveolar progenitors (IAAPs)—a subpopulation characterized by low SFTPC expression but enriched for PD-L1. Single-cell RNA sequencing revealed a reduction in apoptosis among mature AT2 cells. Interestingly, metformin's therapeutic effects were not significantly affected by BMP2 or PPARγ inhibition, which blocked the lipogenic differentiation of myofibroblasts. However, *Fgfr2b* deletion in *Sftpc* lineage cells significantly impaired metformin's ability to promote fibrosis resolution, a process linked to AMPK signaling. In conclusion, metformin alleviates fibrosis by directly activating AT2 cells, especially the IAAPs, through a mechanism that involves AMPK and FGFR2b signaling, but is largely independent of BMP2/PPARγ pathways.

© 2025 The Authors. Published by Elsevier B.V. on behalf of Chinese Pharmaceutical Association and Institute of Materia Medica, Chinese Academy of Medical Sciences. This is an open access article under the CC BY-NC-ND license (http://creativecommons.org/licenses/by-nc-nd/4.0/).

1. Introduction

Idiopathic pulmonary fibrosis (IPF), the most severe form of pulmonary fibrosis, is characterized by progressive and devastating lung dysfunction. With a median survival of 2−3 years after diagnosis, its mortality rate surpasses that of many cancers[1−3]. IPF is characterized by the activation of myofibroblasts (MYFs) and the excessive deposition of extracellular matrix proteins in the lung interstitium, resulting in the destruction of the lung structure and function[4−7]. The pathogenesis of IPF primarily involves chronic alveolar epithelial injury and impaired repair processes, leading to the replacement of the alveolar structure by fibrotic lesions and a honeycomb appearance[8−12]. As such, IPF progression is intricately linked to significant alterations in the proliferation, differentiation, and function of alveolar epithelial cells (AECs)[8,9]. Alveolar type 2 (AT2) cells serve as major facultative stem cells in the adult lung, are capable of self-renewal under homeostatic conditions, and are rapidly activated in response to epithelial injury, contributing to regeneration and repair[13−15]. Wu et al.[16] demonstrated that loss of *Cdc42* in AT2 cells alone is sufficient to drive progressive lung fibrosis, reinforcing the concept that epithelial damage is a primary driver of fibrosis. Given that AT2 cells interact with mesenchymal cells to maintain lung homeostasis, their dysfunction—characterized by impaired self-renewal and differentiation—can perpetuate fibrosis by disrupting epithelial-mesenchymal crosstalk[17−22]. Mesenchymal cells sense AT2 dysfunction through factors such as TGF-β, senescence-associated secretory phenotype, and extracellular vesicles, which can lead to excessive extracellular matrix deposition and fibrosis progression[23−28]. Moreover, epithelial injury initiates local immune responses, triggering inflammatory cascades that activate fibroblasts and promote collagen deposition[29]. Enhancing epithelial repair may indirectly modulate immune responses, reducing pro-inflammatory cytokine production (*e.g.*, IL-1β, TNF-α, and TGF-β) and alleviating chronic inflammation, thereby inhibiting further fibrosis progression. Additionally, epithelial-derived MMP-7 plays a dual role in fibrosis—initially promoting neutrophil infiltration and epithelial damage but later contributing to fibrosis resolution through immune modulation[30−33].

Despite intense research efforts and significant progress in understanding the causes, pathology, and diagnosis of IPF[7,34], therapeutic advances have been limited since the US Food and Drug Administration approved pirfenidone and nintedanib over a decade ago[35]. A pressing need exists for better, ideally curative therapies. Interestingly, emerging evidence shows that metformin (Met), a first-line antidiabetic drug, exhibits potent antifibrotic properties in various preclinical models. Initial studies showed that reducing TGFβ1-induced fibrosis in human bronchial fibroblasts[36], and subsequent studies, including our own, have shown that Met treatment decreases the expression of profibrotic markers and leads to significant histopathological improvements in various preclinical models[37−42].

A critical observation by Rangarajan et al.[37] indicated that fibroblasts isolated from the lungs of humans with IPF display significantly decreased AMPK activity, pronounced mTOR and HIF-1α activation, and decreased autophagy flux. More importantly, and consistent with prior reports of its anti-inflammatory and antifibrotic effects, Met is found to reverse established fibrosis in a bleomycin (BLM)-induced mouse injury model in an AMPK-dependent manner, which is associated with increased mitochondrial biogenesis and restored sensitivity to apoptosis[37]. Mechanistically, both the AMPK-dependent and AMPK-independent pathways have been implicated in mediating its beneficial effects, including the modulation of metabolic pathways, the inhibition of TGFβ1 and IGF1 activities, and the suppression of collagen formation, while activating the FOXM1, S100A4, and BMP2−PPARγ signaling pathways[37−41].

While most published research has focused on the expression of fibrotic and inflammatory markers and histopathological parameters, a paucity of information addressing the spectrum of Met target cells and their potential interactions within the lung is available. Our previous work has shown that Met induces the lipogenic differentiation of IPF-derived MYFs[38]. Lipofibroblasts (LIFs) are resident alveolar fibroblasts containing lipid droplets that transfer triglycerides to adjacent AT2 cells for incorporation into surfactant production[43−46]. LIFs also serve as niche cells for AT2 stem cells, supporting their maintenance and self-renewal[47,48]. These findings suggest that LIFs are considered to form the mesenchymal ecotone of AT2 stem cells[13,49]. Given the close relationship between LIFs and AT2 cells and the fact that IPF pathogenesis is driven primarily by repetitive alveolar epithelial cell injury, maladaptive repair, and the *trans*-differentiation of fibroblasts to MYFs and subsequent activation, investigating whether Met regulation of LIF-to-MYF *trans*-differentiation impacts AECs to potentially facilitate the reversal or accelerated resolution of established fibrosis is warranted. Interestingly, our recent study revealed the potential ability of Met to mitigate the detrimental effects of carcinogen exposure by inhibiting necroptosis and protecting AT2 cells[42].

In the present study, we employed *Sftpc* lineage tracing and *Fgfr2b* conditional knockout (cKO) mice, combined with pharmacological inhibition of BMP2/PPARγ and AMPK signaling, to

explore Met's impact on AECs in a BLM-induced pulmonary fibrosis model. We further examined its potential influence on AT2 stem cell properties—particularly injury-activated alveolar progenitors (IAAPs), an immature AT2 subpopulation that expands post-injury and aberrantly accumulates in IPF lungs[50−52]. Our results demonstrate that Met enhances the resolution of established fibrosis by directly activating AT2 stem cells, especially the IAAPs, through a mechanism independent of BMP2/PPARγ signaling but dependent on AMPK and FGFR2b signaling pathways.

2. Materials and methods

2.1. Animals and drug administration

Male C57BL/6 mice and *Sftpc*$^{CreERT2/+}$, *tdTomato*$^{flox/+}$, and *Fgfr2b*$^{flox/flox}$ mice, aged 8−12 weeks were used in this study, as previously reported[50,53,54]. The mice were housed in a temperature-controlled facility with a 12 h light/dark cycle and provided food *ad libitum*. All experiments were conducted in accordance with the approval of Institutional Animal Center and Use Committee of The First Affiliated Hospital of Wenzhou Medical University (Permit No.: WYYY- IACUC-AEC-2025-045).

For *Sftpc* promoter-driven lineage tracing, 8- to 10-week-old male mice were administered tamoxifen in corn oil (200 μg/g) *via* intraperitoneal (i.p.) injections every other day for a total of 3 injections. After a 7-day period of washout, a single dose of BLM (1.8 μg/g body weight) was administered *via* intratracheal (i.t.) instillation, and the control mice were administered saline. At 14 or 21 days after BLM injury, we replaced the regular drinking water with water containing Met (1.5 mg/mL). The mice in the Met treatment group were allowed to drink only the Met-containing water until the end of the modelling period. Oleuropein (2 μg/g, MedChemExpress, Shanghai, China), Noggin (0.05 μg/g, MedChemExpress), or PBS was i.t. instilled on Day 21 after BLM injury. The lungs were harvested on Day 28.

2.2. Cell culture and treatment methods

Murine lung epithelial-12 (MLE-12) cells were cultured in DMEM (Gibco, Waltham, MA, USA) supplemented with 10% fetal bovine serum and 1% penicillin−streptomycin (both from Gibco). The cells were divided into four groups: Ctrl, BLM, BLM + Met, and BLM + Met + dorsomorphin (MedChemExpress). After 24 h of serum starvation in DMEM, treatments were applied to all the groups. Treatment conditions are summarized in Supporting Information Table S1.

2.3. Pulmonary function test

The limbs of the mice were fixed on a plate with tape, and the mice were placed in the supine position. The skin of the neck was subsequently cut open to expose the trachea. A needle was inserted between the tracheal cartilage rings, and the other end of the needle was connected to the lung function apparatus through a Y-shaped tube. During the lung function test, the mice were administered aerosolized acetylcholine solutions at different concentrations (3.125, 6.25, 12.5, 25, and 50 mg/mL). The corresponding respiratory resistance (Rrs), elastic resistance (Ers), and respiratory compliance (Crs) at each concentration were recorded by FlexWare Software.

2.4. H&E, Sirius red, Masson's trichrome staining and fibrosis quantification

After deparaffinization, the lung sections were stained with haematoxylin (Beyotime Biotechnology, Shanghai, China) for 8 min, washed with running tap water for 10 min, and then stained with eosin (Beyotime Biotechnology) for 90 s. Sirius red staining was performed using a Sirius red staining kit according to the protocol recommended by the manufacturer (Solarbio, Beijing, China). Collagen staining was performed using a Masson's trichrome staining kit according to the manufacturer's protocol (Solarbio). Fibrosis was assessed with the ImageJ program.

2.5. Tissue and cell immunofluorescence (IF) staining

For IF staining, lung sections were first subjected to deparaffinization and antigen retrieval and then blocked with 3% BSA in PBS supplemented with 0.4% Triton-X (Sigma−Aldrich, St. Louis, MO, USA) for 1 h at room temperature (RT). The samples were subsequently incubated with primary antibodies against RFP (rabbit, 1:200; Rockland Immunochemicals, Limerick, PA, USA), pro-SFTPC (rabbit, 1:100; Abcam), RAGE (rat, 1:100; Santa Cruz Biotechnology, Dallas, TX, USA), PD-L1 (mouse, 1:100; Abcam), PD-L1 (rabbit, 1:100; Abcam), p-AMPK (rabbit, 1:100; Cell Signaling Technology, Danvers, MA, USA), BEK/FGFR2 (mouse, 1:100; Santa Cruz Biotechnology), E-cadherin (rabbit, 1:100; Abcam) and α-smooth muscle actin (α-SMA) (mouse, 1:400; Sigma−Aldrich). The next day, the lung sections were washed with PBS and incubated with secondary antibodies diluted in 1% BSA supplemented with 0.1% Triton-X for 1 h at RT. Finally, the cell nuclei were counterstained with DAPI.

For IF staining of cultured cells, MLE-12 cells in the logarithmic growth phase were plated in a 12-well plate containing coverslips. After drug treatment, the cells from each group were washed with PBS, fixed with paraformaldehyde at RT for 20 min, washed with PBS again, and then blocked with 5% BSA for 1 h. The cells were incubated overnight at 4 °C with primary antibodies against p-AMPK (1:200; Cell Signaling Technology) and BEK/FGFR2 (1:200; Santa Cruz Biotechnology). After being washed with PBS, the cells were incubated with secondary antibodies for 2 h at RT, followed by 3 washes with PBS. The coverslips were then removed and mounted with a mounting medium containing DAPI. Visualization and image capture were performed using a Leica Stellaris 5 confocal microscope, and positive cells were quantified using ImageJ FIJI software.

2.6. Annexin V-FITC/PI, TUNEL, EDU, and hydroxyproline assays

For the Annexin V-FITC/PI assay, a single-cell suspension was prepared and assessed with an Annexin V apoptosis kit according to the manufacturer's instructions (Thermo Fisher Scientific, Waltham, MA, USA).

For the TUNEL assay, lung sections were processed, and apoptotic cells were assessed using a One Step TUNEL Apoptosis Assay Kit (Beyotime Biotechnology), as previously described[42]. TUNEL $^{+}$ cells were counted according to the manufacturer's guidelines, and the nuclei were counterstained with DAPI.

For EDU staining, the mice were administered an i.p. injection of 100 mg/kg EDU (Beyotime Biotechnology) 24 h prior to euthanasia. Lung tissue samples were rapidly frozen in liquid nitrogen and embedded in an OCT compound. IF staining was performed using the BeyoClick™ EDU-488 Cell Proliferation Assay Kit (Beyotime Biotechnology) according to established protocols[42].

For the determination of total hydroxyproline levels, each tissue sample was assessed using a hydroxyproline kit (BioVision, Milpitas, CA, USA) according to the manufacturer's instructions.

2.7. RNA extraction and quantitative real-time PCR (qPCR)

Total RNA was extracted using the TRIzol method (Thermo Fisher Scientific), and cDNA synthesis was performed with a TaKaRa reverse transcription kit according to the manufacturer's instructions (TaKaRa Bio, Shiga, Japan). qPCR was performed using iTaq Universal SYBR Green Supermix (Bio-Rad Laboratories, Hercules, CA, USA) on a LightCycler 480 II machine (Roche Diagnostics, Basel, Switzerland). β-Actin was used as a reference gene. The data are presented as the expression levels relative to that of β-actin using the $2^{-\Delta CT}$ method. The primer sequences are listed in Supporting Information Table S2.

2.8. Western blot (WB) analysis

For WB analysis, dissected lung tissues were homogenized in freshly prepared cell lysis buffer containing a protease inhibitor cocktail (Sigma−Aldrich) and phosphatase inhibitors (Roche Diagnostics). Protein quantification was performed using a bicinchoninic acid protein assay (Beyotime Biotechnology). Samples (20−50 μg) were separated on a 10% SDS-polyacrylamide gel and transferred onto PVDF membranes (Roche Diagnostics). The membranes were blocked with 5% skim milk in Tris-buffered saline at RT on a shaker for 1 h. Primary antibodies, including those against AMPK (1:1000; Abcam), p-AMPK (1:1000; Cell Signaling Technology), BEK/FGFR2 (1:1000; Santa Cruz Biotechnology), E-cadherin (1:1000; Abcam), ADRP (1:1000; Abcam), FGF10 (1:1000; Merck Millipore, Burlington, MA, USA), β-tubulin and β-actin (1:1000; Abcam), were applied and incubated overnight at 4 °C. HRP-conjugated goat anti-mouse or goat anti-rabbit secondary antibodies (1:10,000) were incubated with the membranes at RT for 1 h. Membranes were then treated with AceGlow chemiluminescence substrate (Peqlab Biotechnologie, Erlangen, Germany) and imaged immediately using ChemiDoc XRS + (Bio-Rad Laboratories).

2.9. ELISA

The tissue samples were thoroughly homogenized in an appropriate amount of PBS and centrifuged at 5000×*g* for 5 min. The supernatant was collected, and the assay was conducted using a mouse FGF10 ELISA kit according to the manufacturer's instructions (UpingBio technology, Hangzhou, China).

2.10. Lung dissociation and preparation of single cells

After standard surgical procedures, the lungs were carefully perfused with 5 mL of PBS. A 20 G Angio catheter was used to administer 1 mL of dispase solution in DMEM (1 mg/mL) *via* i.t. cannulation. Next, 0.6 mL of 1% agarose was gently introduced into the lungs through the catheter, followed by a 2-min cooling period on ice. Individual lung lobes were dissected and placed in a 50 mL conical tube with dispase solution and then incubated at RT for 55 min on a rocker at 150 rpm.

The digested lungs were transferred to a 10 cm Petri dish with complete DMEM containing DNase. The lung parenchyma was gently separated from the large airways using sharp tweezers, and the Petri dish was rocked at 60 rpm for an additional 10 min at RT. The airways were removed by sequentially straining the crude single-cell lung suspension through 100-, 70-, and 40-μm strainers. Finally, the cells were centrifuged at 300×*g* at 4 °C, and the resulting pellet was suspended in 500 μL of complete DMEM.

2.11. Magnetic cell sorting and flow cytometry

A MACS® Separator Kit was used to deplete $CD45^+$ and $CD31^+$ cells from lung single-cell suspensions, which were prepared as described above, according to the manufacturer's protocol. Briefly, the cell suspensions were centrifuged, and the supernatant was fully aspirated. CD45 and/or CD31 MicroBeads (Miltenyi Biotec, Bergisch Gladbach, Germany) were added (100 μL per 10 million cells) in MACS buffer (Miltenyi Biotec). The cells were gently mixed and incubated for 15 min at 4 °C, followed by washes with 1 mL of buffer and resuspension in 500 μL of MACS buffer before application onto the column. Unlabeled cells from the flow-through were collected, centrifuged, and resuspended in 200 μL of MACS buffer. The isolated cells were stained with anti-EpCAM (APC-conjugated, 1:50; BioLegend, San Diego, CA, USA) for 45 min and LipidTOX (FITC-conjugated, 1:200; Thermo Fisher Scientific) for 30 min on ice in the dark. The flow cytometry analysis was conducted on an ACEA NovoCyte flow cytometer, and data were analysed using FlowJo software version X.

2.12. Generation and analysis of scRNA-seq data

The isolated cell suspension was loaded onto 10 × Chromium, with approximately 8000 cells expected to be captured during the generation of gel beads-in-emulsions. The procedure followed the manufacturer's instructions for the single-cell 3′ gene expression kit (v3.1) or the single-cell 5′ gene expression kit (v2). Briefly, the gel beads-in-emulsions were first reverse-transcribed to produce first-strand cDNAs, which were then purified with Dynabeads and amplified in 12 cycles to generate double-stranded cDNAs. Next, the dsDNA was fragmented, end-repaired, and further ligated with an adaptor. Finally, index PCR was performed before sequencing. The library was sequenced on the Illumina HiSeq X Ten PE150 platform.

Data were processed using the Cell Ranger software pipeline (version 3.1.0) from 10 × Genomics to demultiplex cellular barcodes, map reads to the genome and transcriptome with the STAR aligner, and downsample reads to create normalized aggregate data across samples, producing a matrix of gene counts versus cells. The unique molecular identifier count matrix was processed using the Seurat R package (version 5.0.3).

To filter out low-quality cells and potential multiplet captures, we applied a criterion based on unique molecular identifier/gene numbers, setting a threshold of the mean ± 2 standard deviations. Cells with fewer than 500 unique genes or a total RNA count below 1000 were excluded. Cells with fewer than 500 unique genes or a total RNA count of less than 1000 were removed. Cells with RNA counts above 20,000, which may indicate doublets, were also excluded. Additionally, cells with 10% or more mitochondrial genes were filtered out due to potential cell stress or

damage. After filtering, library size normalization was performed in Seurat to obtain normalized counts.

To identify highly variable genes, principal component analysis was performed using the RunPCA function, and significant principal components were identified with ElbowPlot. Eventually, a total of 20 principal components were used as input for RunUMAP, and clustering was performed with the FindClusters with a parameter resolution = 0.1.

Differentially expressed genes were identified using DESeq2 (version 1.42.1) package in R, with thresholds of an adjusted *P* value < 0.05, $|\log_2\text{fold change}| > 1$, and base mean expression >1 for further pathway enrichment analyses. A Gene Ontology enrichment analysis was conducted to identify the biological pathways significantly affected by the differentially expressed genes, and the enriched Gene Ontology terms from the ClusterProfiler package (version 4.10.1) were used. Gene expression data were extracted using FetchData from the Seurat package, and a heatmap was created using geom_tile from the ggplot2 package (version 3.5.0).

2.13. Quantification and statistical analysis

The quantification of IF images involved counting the number of cells in five independent 40 × fields per sample. Fibrosis in H&E-stained sections was assessed using the Ashcroft score. The ImageJ FIJI program was utilized to isolate and calculate positive areas for Masson's trichrome and IHC staining. Statistical analyses and graph creation were performed with GraphPad Prism 8 (GraphPad Prism Software, San Diego, CA, USA). Statistical significance was determined using unpaired two-tailed Student's tests, and the data are presented as the mean ± standard error of the mean (SEM). A *P*-value of <0.05 was considered statistically significant. The number of biological samples (*n*) for each group is specified in the respective figure legends. Significance levels are denoted as follows: $*P < 0.05$; $**P < 0.01$; $***P < 0.001$; and $****P < 0.0001$.

3. Results

3.1. Met accelerates the resolution of BLM-induced pulmonary fibrotic lesions and functional recovery

To evaluate the effect of Met on established pulmonary fibrosis, we administered Met starting on Day 21 post-BLM treatment (BLM-dpi21) and assessed its effects on lung function and fibrosis resolution at BLM-dpi28, as depicted in Fig. 1A. Changes in body weight dynamics and pulmonary function parameters, including Rrs, Ers, and Crs, were carefully recorded.

Mice exposed to BLM exhibited progressive weight loss up to BLM-dpi28, whereas those treated with Met beginning at dpi21 showed rapid body weight recovery (Fig. 1B). Pulmonary functional tests revealed elevated Rrs and Ers values across different acetylcholine concentrations in BLM-treated mice compared with those in control mice or mice treated with Met alone (Fig. 1C and D). Notably, the BLM(B) + Met(M) group presented significantly lower Rrs and Ers levels than the BLM-only group did, with Rrs and Ers levels near those observed in control or Met-treated mice, indicating improved lung function. Metformin treatment slightly increased the Crs level, but this difference did not reach statistical significance (Fig. 1E). Together, these results demonstrate that Met alleviates BLM-induced body weight loss and improves lung function parameters.

Further analysis revealed a substantial reduction in the hydroxyproline content in the B + M group compared with the BLM group (Fig. 1F). Histopathological examinations with H&E, Sirius Red, and Masson's trichrome staining consistently revealed less dense fibrotic tissue and collagen deposition in Met-treated mice than in those treated with BLM alone. This was corroborated by a lower Ashcroft fibrosis score, as well as reduced Sirius Red staining (% positive area) and Masson's trichrome staining (% positive area) in the Met-treated mice (Fig. 1G−L). These findings were validated by extended observations until dpi56, which revealed sustained fibrosis resolution with Met treatment (Supporting Information Fig. S1). Furthermore, administration of Met at dpi14 after BLM injury produced similar results, with H&E and Masson's trichrome staining, as well as hydroxyproline assays, indicating the effective alleviation of pulmonary fibrosis (Supporting Information Fig. S2).

Collectively, these results provide strong evidence that Met administration not only accelerates the resolution but also reduces the severity of pulmonary fibrosis. These improvements are accompanied by enhanced lung function parameters and reductions in the levels of histological markers of fibrosis.

3.2. Met ameliorates BLM-induced fibrosis and promotes mature AT2 marker expression and alveolar repair

Given the genetic and experimental evidence linking chronic or repetitive AEC damage and impaired respiratory epithelial repair to disease pathogenesis, we sought to determine whether Met aids in the recovery of BLM-induced epithelial injury.

First, we assessed AMPK activation in mouse lung tissues using the experimental scheme outlined in Fig. 1A. The immunoblot analysis revealed a marginal increase in phospho-AMPK levels in Met-treated control mice, whereas BLM treatment significantly decreased its activation (Fig. 2A and B). Notably, Met administration to BLM-injured mice significantly restored AMPK activation levels. Furthermore, in contrast to the substantial reduction in E-cadherin levels observed in the BLM group, mice in the B + M group presented a marked increase in E-cadherin expression (Fig. 2A and C). The impact of BLM and/or Met on the mRNA expression of epithelial and fibrosis markers was further confirmed by qPCR (Fig. 2D). Met treatment partially reversed the BLM-induced upregulation of *Acta2* and *Col1a1* and significantly restored BLM-induced decreases in *Cdh1* levels in lung tissues. Additionally, BLM treatment dramatically reduced the levels of the key *Bmp2* and *Pparg* mRNAs previously implicated in driving MYF to LIF differentiation, which was largely restored to control levels by Met. This finding was consistent with the increased expression of *perilipin 2* (*Plin2*), an adipose differentiation-related protein that was downregulated by BLM treatment (Fig. 2D).

AT2 cells serve as primary stem cells in the adult lung for self-renewal and injury-induced regeneration. Therefore, we also performed qPCR analysis of the *Sftpc* mRNA and revealed its upregulation in the B + M group, in contrast to the significant decrease in the BLM injury group, indicating a protective effect of Met on AT2 cells. Similarly, the expression of *Etv5,* crucial for lung branching morphogenesis and AT2 cell identity, was drastically downregulated by BLM injury but was significantly rescued by Met treatment (Fig. 2D).

We next performed IF staining for epithelial markers (E-cadherin for epithelial cells, SFTPC for AT2 cells, and RAGE for AT1

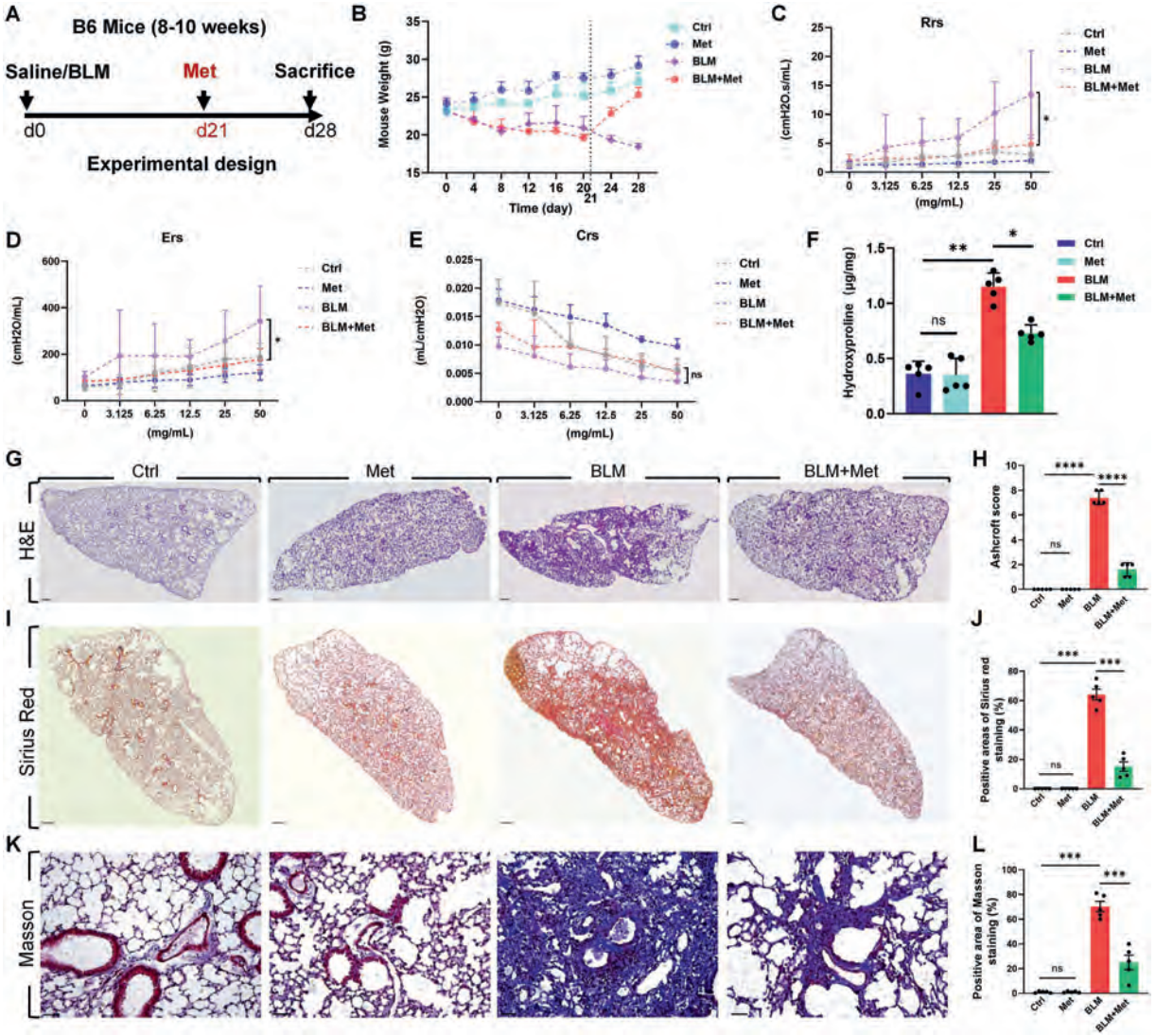

Figure 1 Met accelerates the resolution of BLM-induced lung fibrotic lesions and functional recovery. (A) Timeline of BLM and Met treatments. Saline or BLM was administered *via* an airway drip. The Met and BLM + Met groups were provided water supplemented with Met at 21 dpi post-BLM injury. The mice were sacrificed 28 days after BLM injury. (B) Statistical analysis of the time-dependent weight changes in each group of mice ($n = 3$). (C−E) Statistical graphs of Rrs for mouse lung function, Ers and Crs in the respiratory system ($n = 3$). (F) Graph of the hydroxyproline content ($n = 5$). (G) Images of H&E staining of the lung tissues. Scale bar: 200 μm. (H) Ashcroft score based on H&E-stained sections ($n = 5$). (I) Images of Sirius red staining of lung tissues. Scale bar: 200 μm. (J) Measurement of areas with Sirius red-positive staining ($n = 5$). (K) Images of Masson's trichrome staining of lung tissues. Scale bar: 50 μm. (L) Quantification of Masson's trichrome-stained areas ($n = 5$). The data are presented as the mean ± SEM. Statistical significance is denoted as follows: ns, not significant; $^{*}P < 0.05$, $^{**}P < 0.01$, $^{***}P < 0.001$, and $^{****}P < 0.0001$.

cells) in lung sections to further investigate the impacts of BLM and/or Met treatment on epithelial cells. In the Met-only treated groups, E-cadherin-, SFTPC- and RAGE-positive cells with normal expression levels and distribution were observed and were comparable to those in the control lungs (Supporting Information Fig. S3A and S3B, Fig. 2E). In contrast, the BLM group presented markedly fewer positive cells and a markedly lower intensity of E-cadherin, SFTPC, and RAGE staining. However, in the B + M group, the number of positive cells and the expression levels of E-cadherin, SFTPC, and RAGE were significantly elevated (Fig. S3B, Fig. 2E and F), underscoring the reparative effect of Met on epithelial damage following BLM-induced lung injury. The flow cytometry analysis of lung single-cell suspensions revealed that epithelial cells constituted 17.6% of cells in the control mice. Treatment with BLM alone reduced this proportion to 5.92% within epithelial subpopulations. Notably, the combined BLM and Met treatment significantly increased epithelial cell populations to 10.3% (Fig. S3C and S3D).

These findings collectively indicate that Met significantly activates the AMPK pathway in the lung, enhances the resolution of fibrosis, and promotes alveolar repair in the context of BLM-induced lung injury.

3.3. Met promotes the proliferation and differentiation of AT2 cells, particularly IAAPs

We next assessed the effect of Met on AT2 cells *via* lineage tracing in *Sftpc*$^{CreERT2/+}$; *tdTomato*$^{flox/+}$ mice. Following

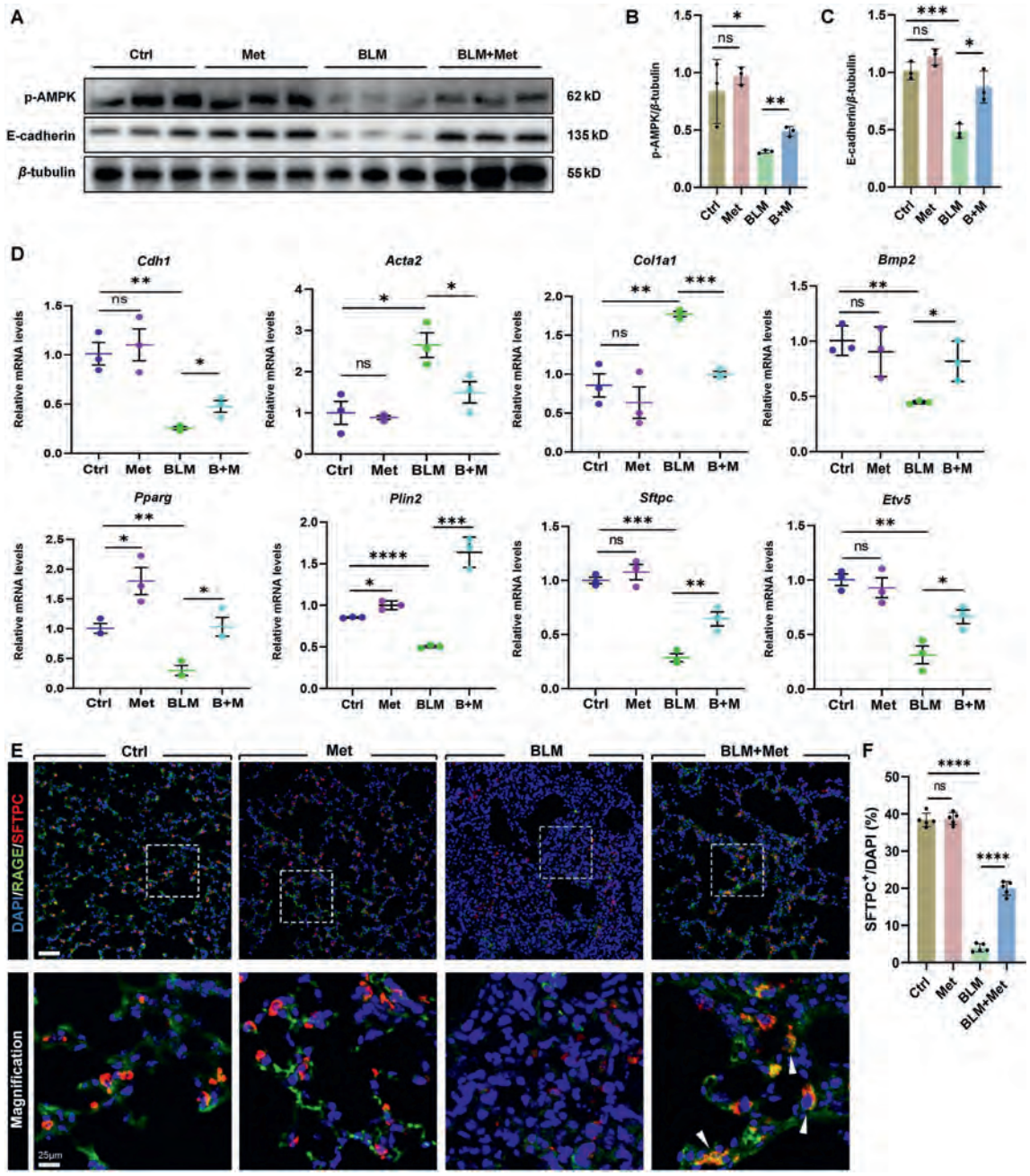

Figure 2 Met ameliorates BLM-induced fibrosis and promotes mature AT2 marker expression and alveolar repair. (A) Immunoblot validation of p-AMPK and E-cadherin protein levels in each group. (B, C) Quantitative analysis of the immunoblot results ($n = 3$). (D) qPCR analysis of *Cdh1*, *Acta2*, *Col1a1*, *Bmp2*, *Pparg*, *Plin2*, *Sftpc*, and *Etv5* expression levels in lung tissues from each group ($n = 3$). (E) IF staining for RAGE and SFTPC in the lungs of wild-type mice that received BLM at 2 months of age and were harvested at 28 dpi. Scale bar: 100 μm. (F) Quantification of $SFTPC^+$ cells among the total cells based on positive fluorescence staining ($n = 5$). The data are presented as the mean ± SEM ns: not significant; $*P < 0.05$, $**P < 0.01$, $***P < 0.001$, and $****P < 0.0001$.

tamoxifen induction and subsequent BLM injury, the mice received Met treatment at BLM-dpi21, with EDU administered at BLM-dpi27 (Fig. 3A). Lung single-cell suspensions were analyzed *via* flow cytometry to measure tdTomato $(Tom)^{low}$ (IAAPs) and Tom^{high} (mature AT2) cell proportions within the epithelial population. In control mice, IAAPs and Tom^{high} AT2 cells accounted for 9.96% and 33.9% of $CD31^-/CD45^-/EpCAM^+$ cells, respectively. Met treatment alone resulted in proportions of 7.98% and 30% for these subpopulations, which were comparable to those of the controls (Fig. 3B). Conversely, BLM-injured mice presented an increase in the proportion of IAAPs and a decrease in the proportion of Tom^{high} cells (9.58% and 22.7%, respectively), which is consistent with previous findings of IAAP activation during injury. Notably, the combined BLM and Met treatment significantly increased the populations of IAAPs and Tom^{high} cells to 34.6% and 38.1%, respectively (Fig. 3B−D).

Given that IAAPs are injury-activated AT2 stem cells enriched for PD-L1 expression, we performed IF co-staining for EDU and

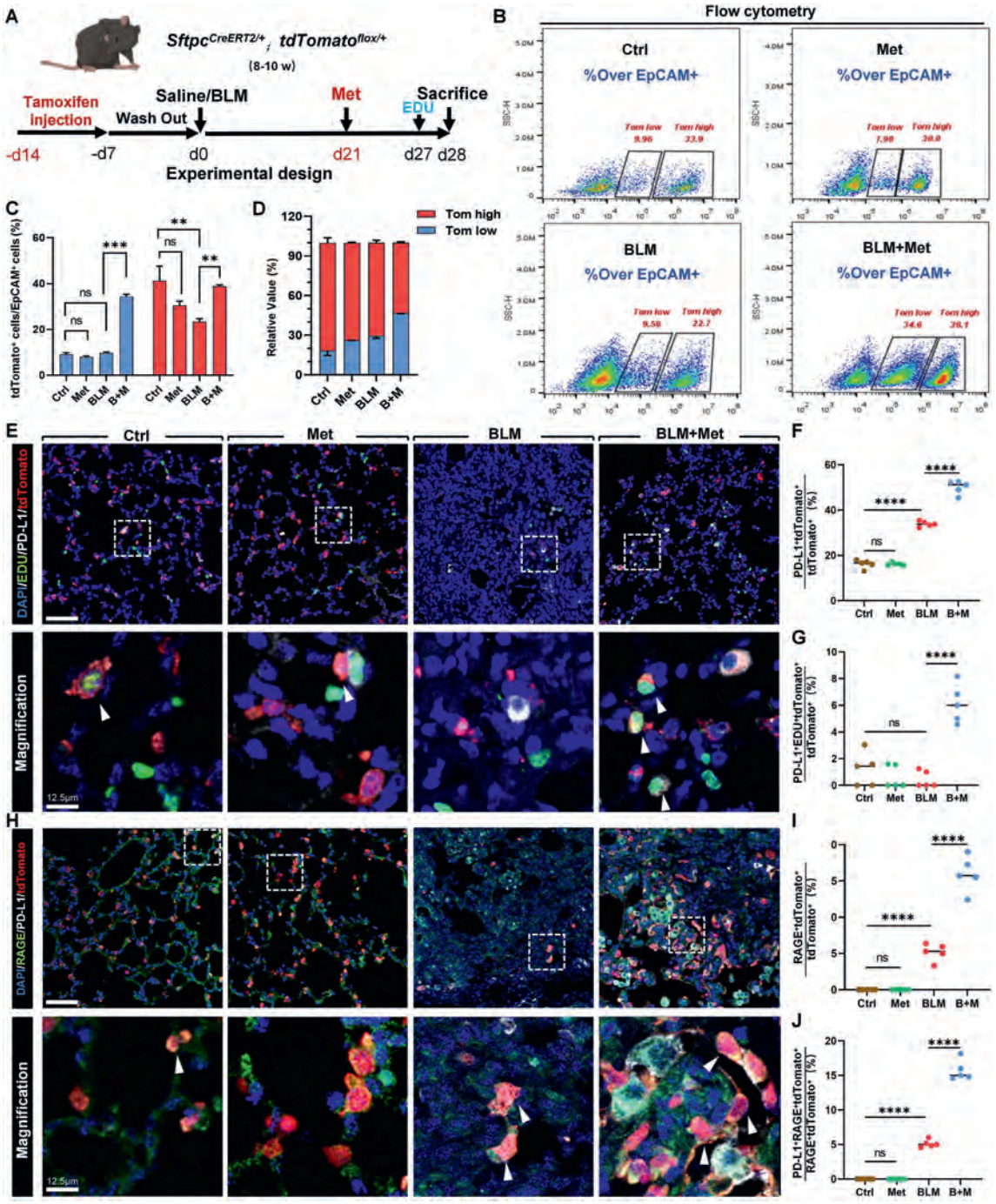

Figure 3 Met promotes the proliferation and differentiation of AT2 cells, particularly IAAPs. (A) Timeline of BLM and Met treatments. The mice were sacrificed 28 days after BLM administration and were i.p. injected with EDU the day before sacrifice. (B) Representative FACS analysis of IAAPs and AT2 cells in each group. (C) Quantification of the percentage of tdTomato$^+$ cells among EpCAM$^+$ cells ($n = 3$). (D) Quantification of the percentages of Tom^{low} and Tom^{high} cells ($n = 3$). (E) Immunostaining for PD-L1$^+$ and EDU in the lungs of the *Sftpc*$^{CreERT2/+}$*; tdTomato*$^{flox/+}$ mice in each group. Scale bar: 50 μm. (F) Quantification of the immunofluorescence data showing the percentage of PD-L1$^+$ cells among the total number of tdTomato$^+$ cells ($n = 5$). (G) Quantification of the immunofluorescence data showing the proportion of proliferating PD-L1$^+$ cells among the tdTomato$^+$ cells ($n = 5$). (H) Immunostaining for PD-L1 and RAGE in the lungs of the *Sftpc*$^{CreERT2/+}$*; tdTomato*$^{flox/+}$ mice in each group. Scale bar: 50 μm. (I) Quantification of the immunofluorescence data showing the proportion of RAGE$^+$ cells among the total tdTomato$^+$ cells ($n = 5$). (J) Quantification of immunofluorescence data showing the percentage of RAGE/PD-L1/tdTomato triple-positive cells among RAGE/tdTomato double-positive cells ($n = 5$). The data are presented as the mean ± SEM. ns: not significant; $^{**}P < 0.01$; $^{***}P < 0.001$; and $^{****}P < 0.0001$.

PD-L1 in lung tissue sections and revealed increased IAAP proliferation and PD-L1 positivity within tdTomato-labeled cells in the BLM + Met group compared with those in the BLM alone group (Fig. 3E−G). Additional co-staining for RAGE and PD-L1 revealed a similar increase in the number of RAGE- and PD-L1-positive cells within the tdTomato-labeled population in the BLM + Met group compared with that in the BLM alone group (Fig. 3H−J). The results together suggest Met promotes AT2 cell proliferation, particularly within the IAAP population, and enhances their differentiation towards AT1 cells.

3.4. BMP2/PPARγ activation-induced lipogenic differentiation is not essential for AT2 stem cell activation or alveolar repair

Met has been shown to upregulate BMP2, promoting lipogenic differentiation *via* PPARγ activation in IPF-derived fibroblasts *in vitro*, independent of AMPK signaling[38]. To explore the potential role of BMP2/PPARγ signaling in regulating alveolar stem cell activity and its contribution to Met's therapeutic effects *in vivo,* we administered noggin and oleuropein, inhibitors of BMP2 and PPARγ, respectively, to *Sftpc* lineage-traced mice treated with BLM and/or Met (Fig. 4A). H&E, Masson's trichrome, and IF staining confirmed the lack of discernible biological toxicity when Met, noggin, or oleuropein was administered alone at the indicated doses to control mice (Supporting Information Fig. S4). Although Met alone did not significantly alter *Bmp2* or *Pparg* expression in lung tissues in control mice, noggin or BLM treatment markedly reduced their levels. Interestingly, Met treatment nearly restored *Bmp2* expression in BLM-injured mice to control levels (Fig. 4B). Similarly, oleuropein or BLM alone significantly downregulated *Pparg* expression, whereas Met reversed this change towards control levels. The inhibitory effects of noggin and oleuropein were validated, as they attenuated the efficacy of Met on reversing BLM-induced *Bmp2* or *Pparg* downregulation (Fig. 4C).

Next, we further examined the effects of BMP2 and PPARγ inhibition on Met-induced lipogenic differentiation by measuring *Plin2* expression. In the B + M group, the *Plin2* mRNA was significantly upregulated compared with that in the BLM group (B group), whereas the inhibition of BMP2 with Noggin (B + M + N) or PPARγ with oleuropein (B + M + O) signaling reduced *Plin2* expression compared with that in the B + M group (Fig. 4D). LipidTOX staining showed consistent results, with fewer LipidTOX$^+$ cells in the B+M + N and B + M + O groups than in the B + M group (Supporting Information Fig. S5). In control mice, the proportion of LipidTOX$^+$ cells within the CD31$^-$CD45$^-$EpCAM$^-$ population constituted 18.7%, which decreased to 6.33% in the BLM group (Fig. S5). Notably, the restoration of lipogenic mesenchymal cells by Met in the B + M group was largely attenuated in the presence of BMP2 or in the PPARγ-inhibited groups relative to that in the B + M group (Fig. S5), as further confirmed by WB (Supporting Information Fig. S6A and S6B).

To investigate the impact of BMP2/PPARγ signaling on Met-mediated fibrotic resolution, qPCR was performed and showed decreased *Acta2* and *Col1a1* mRNA expression in the B + M, B + M + O, and B + M + N groups compared to BLM alone (Fig. 4E and F). Additionally, α-SMA expression decreased while E-cadherin expression increased in the B + M, B + M + O, and B + M + N groups (Figs. S6A, S6C, and S6D). Histological analyses, including H&E, Masson's trichrome, and IF staining, were conducted to evaluate whether BMP2/PPARγ pathway inhibition alters the efficacy of Met in mitigating BLM-induced lung injury or fibrosis (Fig. 4G−J). The results showed that BMP2/PPARγ inhibition did not diminish the therapeutic effects of Met (Fig. 4G−J). The results of the hydroxyproline assay are consistent with the histological findings (Fig. 4K). Similarly, α-SMA staining was significantly lower in the B + M group than in the B group, with an increased number of tdTomato-positive cells (Fig. 4L−N). However, no notable differences were observed in the B + M + N and B + M + O groups compared with the B + M group, suggesting that BMP2/PPARγ inhibition did not hinder the ability of Met to promote fibrosis resolution (Fig. 4L−N). Additionally, administration of noggin or oleuropein alone had no significant effect on BLM-induced pulmonary fibrosis, as shown by H&E staining, Masson's trichrome staining, and hydroxyproline assays (Supporting Information Fig. S7).

These findings provide direct evidence that while BMP2/PPARγ signaling contributes to Met-induced lipogenic differentiation in BLM-induced fibrosis, it does not appear to be essential for the Met-mediated acceleration of fibrosis resolution in this model.

3.5. Met activation of alveolar epithelial stem cells is independent of BMP2/PPARγ signaling

Newly generated LIFs are known to constitute a niche of AT2 cells. Given that BMP2/PPARγ signaling inhibitors effectively suppress the lipogenic differentiation of MYFs *in vitro*, we explored whether BMP2/PPARγ signaling plays a role in alveolar epithelial cell regeneration, with a specific focus on the IAAP subpopulation, which is known for its survival advantage and dynamic expansion following PNX and BLM injury[38,50,51]. *Sftpc* lineage-traced (*Sftpc$^{CreERT2/+}$; tdTomato$^{flox/+}$*) mice were induced with tamoxifen and subjected to BLM injury. The mice were subsequently treated with Met alone or in combination with BMP2 (noggin) and PPARγ (oleuropein) inhibitors (Fig. 4A). Lung single-cell suspensions were analysed by flow cytometry to determine the proportions of Tom^{Low} IAAPs and Tom^{high} mature AT2 cells within the epithelial population (CD31$^-$/CD45$^-$/EpCAM$^+$ cells). The results revealed that Met administration beginning at dpi21 post-BLM injury significantly increased the proportions of both IAAPs and mature AT2 cells at dpi28, with a more pronounced increase in the IAAP population (Fig. 5A). Notably, the coadministration of noggin (B + M + N group) did not significantly alter the IAAP proportion compared with that in the B + M group (Fig. 5B). Similarly, the combined treatment with oleuropein (B + M + O group) did not affect IAAP cell proportions compared with those in the B + M group, although a slight reduction in the proportion of Tom^{high} mature AT2 cells was observed (Fig. 5B and C).

The IF analysis further revealed a significant increase in the proportion of PD-L1$^+$ tdTomato$^+$ cells in the B + M group compared to the BLM-alone group, indicating increased AT2 cell proliferation following Met treatment (Fig. 5D). However, no significant differences were detected in the proportions of PD-L1$^+$ tdTomato$^+$ cells within the tdTomato$^+$ population and PD-L1$^+$ EDU$^+$ tdTomato$^+$ cells within the tdTomato$^+$ population among the B + M, B + M + N, and B + M + O groups (Fig. 5E and F). Additional co-staining for RAGE and PD-L1 showed a similar increase in RAGE and PD-L1 positive cells within the tdTomato-labeled population in the BLM + Met group compared to BLM alone (Fig. 5G). Similarly, no significant differences were detected in the proportion of RAGE$^+$ tdTomato$^+$ cells within the

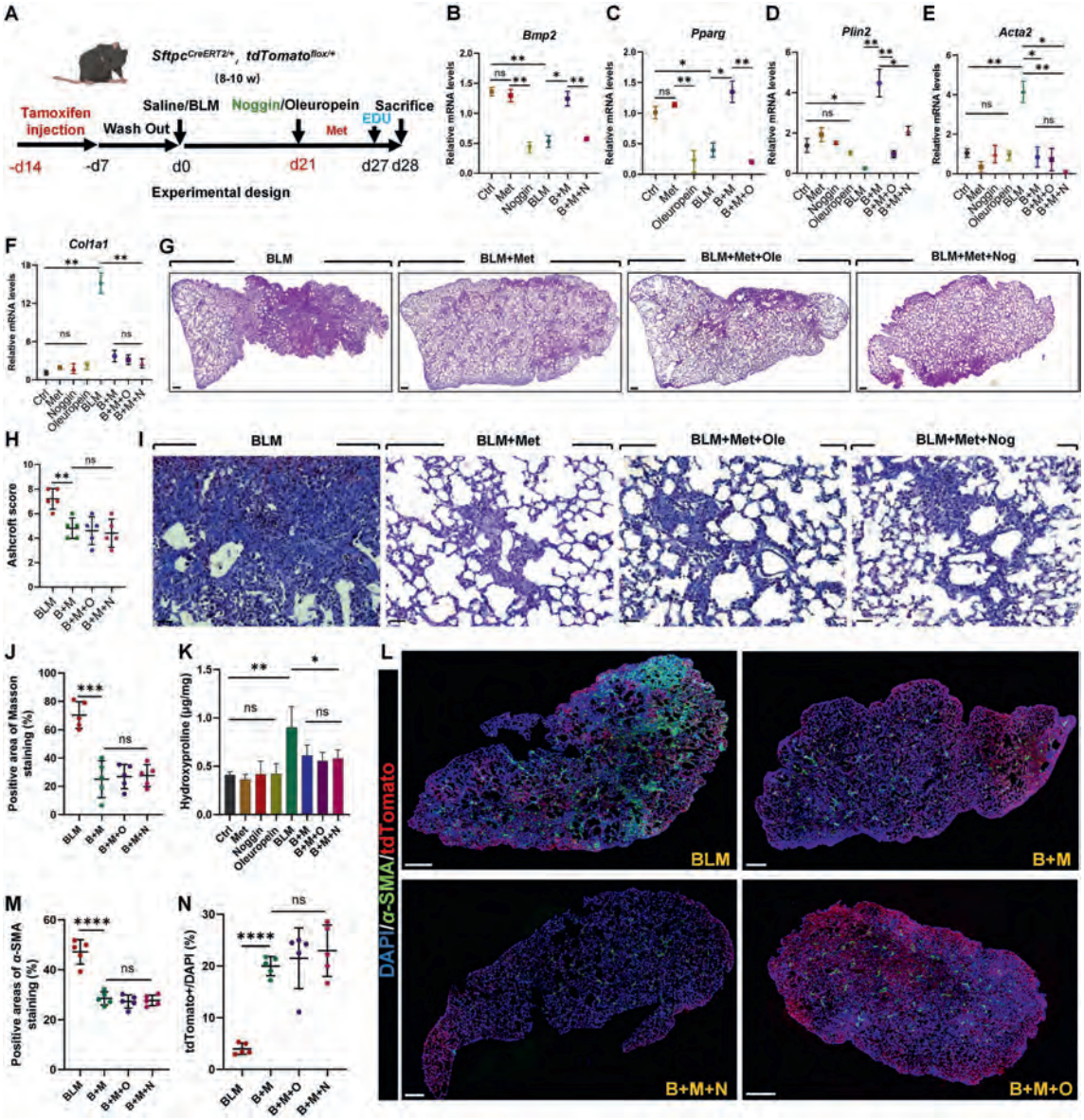

Figure 4 Activation of BMP2/PPARγ signaling contributes to lipogenic differentiation but is not essential for alveolar repair or fibrosis resolution. (A) Timeline and scheme of combined treatment with BLM, Met, and Noggin or Oleuropein. The mice were sacrificed at dpi28 after BLM injury and were i.t. injected with EDU the day before sacrifice. (B−F) qPCR analysis of *Bmp2*, *Pparg*, *Plin2*, *Acta2*, and *Col1a1* expression levels in lung tissues from each group ($n = 3$). (G) H&E staining of lung tissues from each group. Scale bar: 200 μm. (H) Semiquantitative analyses of H&E staining using the Ashcroft score ($n = 5$). (I) Masson's trichrome staining of lung tissues from each group. Scale bar: 50 μm. (J) ImageJ quantification of fibrotic regions based on Masson's trichrome staining ($n = 5$). (K) Quantification of the hydroxyproline content in each group ($n = 5$). (L) Tile scans of the left lung lobes from each group. Lung sections were stained with anti-α-SMA antibodies (green), and the endogenous tdTomato signal (red) was detected. Scale bar: 500 μm. (M) Quantification of the immunofluorescence image showing the α-SMA-positive area ($n = 5$). (N) Quantification of the immunofluorescence data showing the number of lineage-labeled cells in the indicated groups of mice ($n = 5$). The data are presented as the mean ± SEM. ns: not significant; $^*P < 0.05$, $^{**}P < 0.01$, $^{***}P < 0.001$, and $^{****}P < 0.0001$.

tdTomato$^+$ cells and PD-L1$^+$ RAGE$^+$ tdTomato$^+$ cells within the RAGE$^+$ tdTomato$^+$ population among B+M, B + M + N, and B + M + O groups (Fig. 5H and I). This suggests that BMP2 or PPARγ inhibition does not significantly affect the ability of Met to promote AT2 cell proliferation, particularly within the IAAP population, nor their ability to differentiate towards AT1 cells (Fig. 5D−I).

Collectively, the above data suggest that Met robustly activates AT2 stem cell potential, particularly the IAAP subpopulation, independent of the BMP2/PPARγ signaling, which is otherwise associated with the promotion of lipogenic differentiation in MYFs.

3.6. Met-enhanced fibrosis resolution is associated with attenuated AT2 cell apoptosis

To investigate the molecular mechanisms underlying Met-mediated activation of AT2 cells, *Sftpc* lineage tracing mice

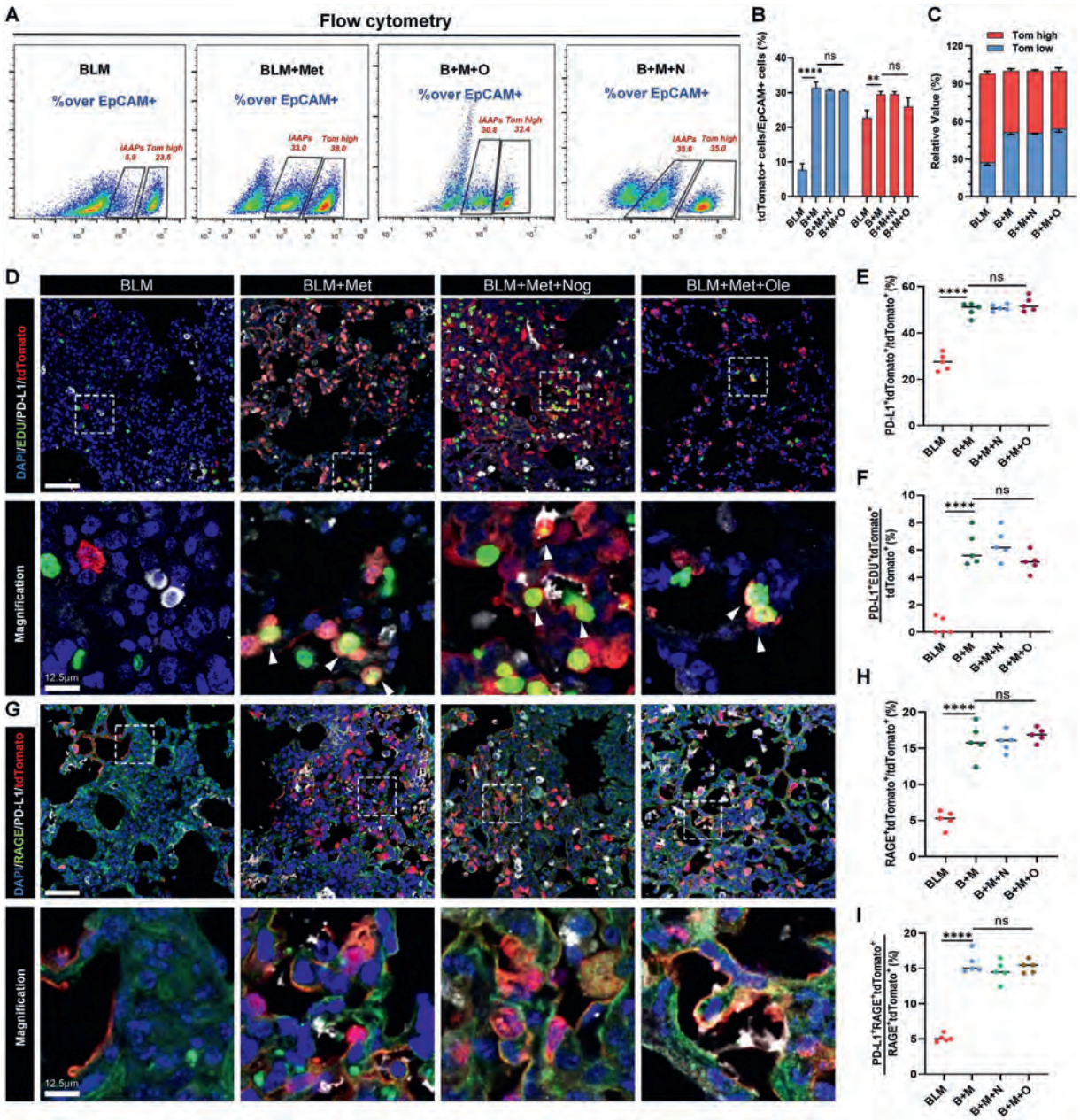

Figure 5 BMP2/PPARγ activation-induced lipogenic differentiation is not essential for AT2 stem cell activation or alveolar repair. (A) Representative FACS analysis of IAAPs and AT2 cells in each group. B. Quantification of the percentages of Tom^{High} and Tom^{Low} cells among EpCAM $^{+}$ cells based on a FACS analysis ($n = 3$). (C) Quantification of the relative percentage of Tom^{Low}/Tom^{High} cells *via* FACS analysis ($n = 3$). (D) Immunostaining for PD-L1 and EDU in *Sftpc* lineage-traced tdTomato^{+} cells in mouse lungs of each group as indicated. Scale Bar: 50 μm. (E) Quantification of the immunofluorescence data showing the percentage of PD-L1^{+} cells out of total tdTomato^{+} cells ($n = 5$). (F) Quantification of immunofluorescence data showing the proportion of proliferating PD-L1^{+} cells out of tdTomato^{+} cells ($n = 5$). (G) Immunostaining for PD-L1 and RAGE in *Sftpc* lineage-traced tdTomato^{+} cells in mouse lungs of each group as indicated. Scale Bar: 50 μm. (H) Quantification of the immunofluorescence data showing the proportion of RAGE^{+} tdTomato^{+} cells out of total tdTomato^{+} cells ($n = 3$). (I) Quantification of immunofluorescence data showing the percentage of RAGE/PD-L1/tdTomato triple positive cells out RAGE/tdTomato double positive cells ($n = 3$). The data are presented as the mean ± SEM. ns: not significant; $^{*}P < 0.05$, $^{**}P < 0.01$, and $^{****}P < 0.0001$.

were induced with tamoxifen and subjected to BLM injury, followed by treatment with Met (B + M group) or no treatment (BLM group) as outlined in Fig. 3A. Single-cell suspensions were isolated from the lungs of both groups on day 28 post-BLM injury. CD31^{+} and CD45^{+} cells were removed *via* MACS, followed by FACS sorting of labeled AT2 cells, including both Tom^{Low} IAAPs and Tom^{high} mature AT2 cells, for scRNA-seq (Fig. 6A).

UMAP analysis identified a total of 9 clusters encompassing known *Sftpc*$^{+}$ subpopulations, including IAAP (quiescent IAAP), *Ki67*$^{+}$ IAAP, *Id2*$^{+}$ IAAP, AT2, *Ki67*$^{+}$ AT2, *Sca-1*$^{+}$ AT2,

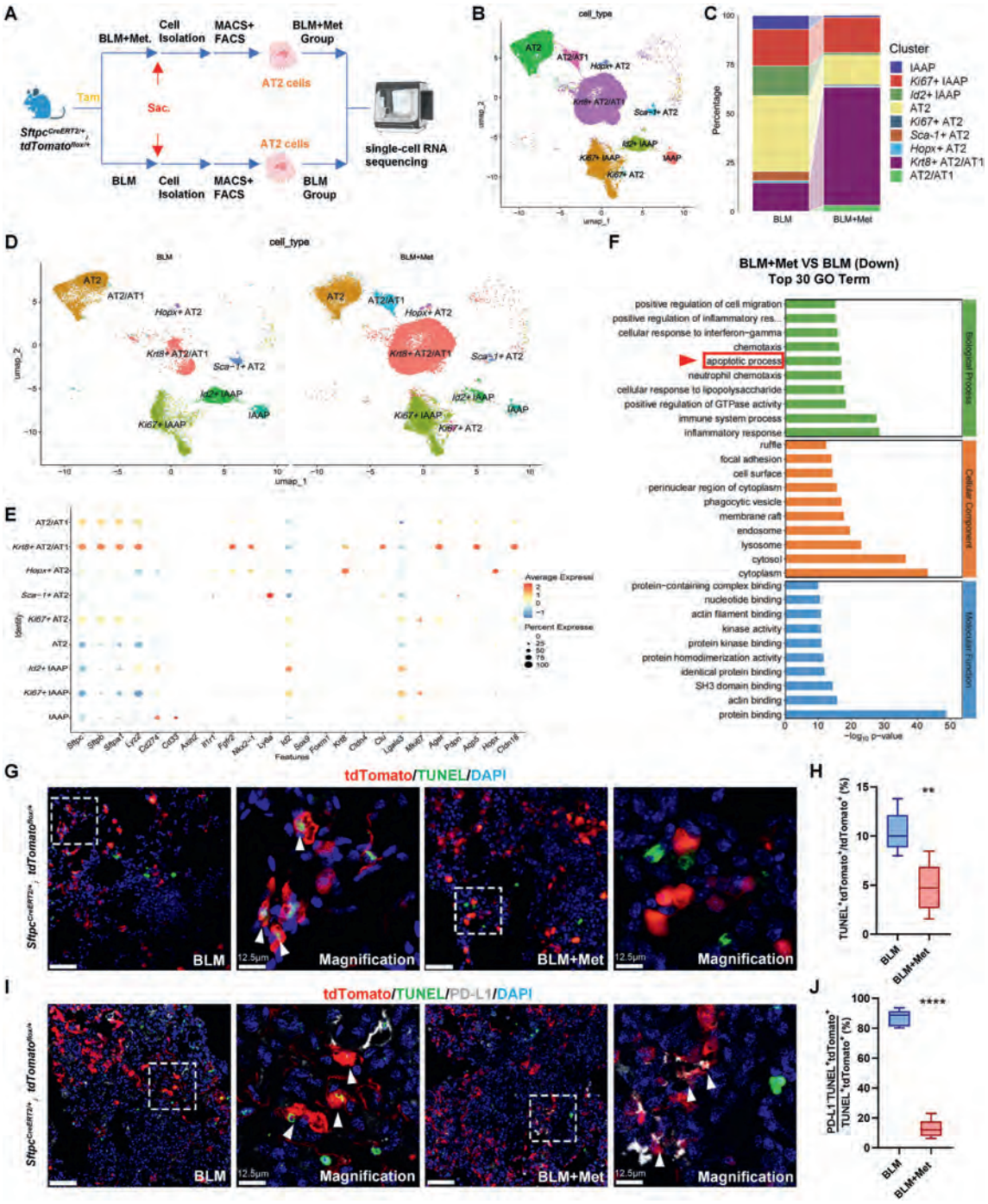

Figure 6 Met-enhanced fibrosis resolution is associated with attenuated AT2 cell apoptosis. (A) *Sftpc* lineage-traced tdTomato reporter mice were used to generate the BLM and B + M groups separately. The cells were isolated from each group, and the $CD31^+$ and $CD45^+$ cells were removed *via* MACS. FACS sorting was used to isolate all the $tdTomato^+$ cells for scRNA-seq. (B) UMAP representation of the scRNA-seq data categorized by cell type. (C) Stacked bar graphs depicting the contributions of each group to the identified clusters. (D) UMAP representation of the scRNA-seq data from both groups stratified by cell type. (E) Heatmap showing the gene expression of the IAAP, $Ki67^+$ IAAP, $Id2^+$ IAAP, AT2, $Ki67^+$ AT2, $Sca\text{-}1^+$ AT2, $Hopx^+$ AT2, $Krt8^+$ AT2/AT1 and AT2/AT1 cell signatures in the BLM and B + M groups. (F) GO analysis of intracluster gene expression in AT2 cells from the BLM and B + M groups. (G) Immunofluorescence co-staining with TUNEL in the BLM and B + M groups. Scale bar: 50 μm. (H) Statistical graph showing the proportion of $TUNEL^+$ cells among the $tdTomato^+$ cells in each group ($n = 5$). (I) Immunofluorescence co-staining for TUNEL and PD-L1 in the BLM and B + M groups. Scale bar: 50 μm. (J) Statistical graph showing the proportion of PD-$L1^-$ $TUNEL^+$ cells among the total $tdTomato^+$ cells in each group ($n = 5$). The data are presented as the mean ± SEM. ns: not significant. $^{**}P < 0.01$, $^{****}P < 0.0001$.

Hopx$^+$ AT2, *Krt8*$^+$ AT2/AT1, and AT2/AT1 cells (Fig. 6B). Fig. 6C shows the relative contributions of the BLM and BLM + Met groups to each cluster. Notably, the BLM + Met group contained a greater number of *Ki67*$^+$ IAAP cells than the BLM group did, indicating the enhanced survival and proliferative capacity of *Pd-l1*$^+$ IAAPs. Additionally, the B + M group uniquely displayed a distinct cluster of *Ki67*$^+$ AT2 cells and an increased presence of intermediate AT2/AT1 cells, such as *Krt8*$^+$ AT2/AT1 cells and AT2/AT1 cells (Fig. 6D).

Met treatment also led to an increase in *Hopx*$^+$ AT2 cells, suggesting increased proliferation and differentiation in response to injury (Fig. 6D). Conversely, a decrease in the number of *Sca-1*$^+$ AT2 cells was observed in the B + M group, potentially reflecting differentiation into other cell populations under the influence of Met (Fig. 6D). The heatmap analysis highlighted unique gene expression profiles across IAAP, *Ki67*$^+$ IAAP, *Id2*$^+$ IAAP, AT2, *Ki67*$^+$ AT2, *Sca-1*$^+$ AT2, *Hopx*$^+$ AT2, *Krt8*$^+$ AT2/AT1, and AT2/AT1 cells in both the BLM and BLM + Met datasets (Fig. 6E). Functional analysis revealed a significant reduction in apoptosis-related processes among AT2 cells in the BLM + Met group compared to BLM group (Fig. 6F).

To validate the effect of Met on epithelial cell survival, lung single-cell suspensions were isolated. EpCAM$^+$ cells were obtained using MACS followed by Annexin-V and PI staining and flow analysis. Annexin V and PI double-positive late apoptotic cells accounted for 3.9% of cells in the control group, which increased to 26.8% in the BLM group and decreased to 17.1% in the B + M group (Fig. S3E). Statistical analysis confirmed that epithelial cell apoptosis was significantly decreased in the B + M group compared to the BLM group (Fig. S3F). IF co-staining with TUNEL revealed a reduction in apoptosis among the tdTomato$^+$ cells, which decreased from 11±2.8% in the BLM group to 4±1.5% in the BLM + Met group (Fig. 6G and H). Notably, mature AT2 cells exhibited significant co-staining with TUNEL, indicating apoptosis, whereas IAAP cells in the BLM + Met group were predominantly PD-L1$^+$ without TUNEL positivity, suggesting a protective effect of Met on IAAPs during injury repair (Fig. 6I and J).

Overall, these findings suggest that Met promotes the proliferation and differentiation of AT2 cells, particularly IAAPs, while mitigating AT2 cell apoptosis.

3.7. Met activation of AT2 stem cell activity requires FGFR2b signaling

Met activation of AT2 stem cell activity correlates with improved alveolar repair, an effect unimpeded by BMP2 or PPARγ inhibitors that otherwise reverse lipogenic differentiation induction. These findings suggest that epithelial cells, especially IAAPs, play a critical role in mediating the positive effects of Met on lung repair and fibrosis resolution.

IAAP cells constitute a transcriptionally stable subpopulation distinct from mature AT2 cells, which express high levels of *Sftpc*, *Etv5*, and *Fgfr2b* and are characterized by enriched *Pd-l1* expression[55]. During PNX, BLM injury, and human IPF, the IAAP subpopulation is significantly activated[50−52]. Importantly, recombinant FGF10 enhances both the peak ratio and duration of IAAP expansion after BLM injury[51]. Furthermore, deletion of *Fgfr2b* in *Sftpc* lineage cells induces apoptosis in mature AT2 cells, accompanied by a compensatory expansion of IAAPs transitioning towards mature AT2 cells[56], underscoring the critical role of FGF10/FGFR2b signaling in AT2 cell survival and IAAP mobilization post-injury. We hypothesize that FGFR2b might contribute to the effects of Met on AT2 and IAAP proliferation in alveolar repair. Therefore, *Sftpc* lineage-traced *Fgfr2b* cKO mice (*Sftpc*$^{CreERT2/+}$; *tdTomato*$^{flox/+}$; *Fgfr2b*$^{flox/flox}$) were induced with tamoxifen, and *Fgfr2b* deficiency was confirmed by IF co-staining with FGFR2 and E-cadherin (Supporting Information Fig. S8A−S8C). The Masson's trichrome and H&E staining, along with hydroxyproline assays, demonstrated that BLM-induced injury in tamoxifen-treated mice led to a more pronounced fibrotic phenotype compared to the control group. (*Sftpc*$^{CreERT2/+}$; *tdTomato*$^{flox/+}$) (Fig. S8D−S8I).

We then subjected *Fgfr2b* cKO mice to BLM injury and Met treatment (Fig. 7A). TUNEL staining revealed a significant fraction of apoptotic AT2 cells in both the BLM alone and BLM + Met groups, with no significant difference in the number of TUNEL$^+$ cells among the tdTomato$^+$ population (Fig. 7B and C). This result contrasted with the findings from *Fgfr2b* wild-type mice, where Met treatment reduced the percentage of TUNEL$^+$ cells by 50% (from 10% to 5%, Fig. 6G and H), indicating that FGFR2b activation contributed to the antiapoptotic effect of Met on AT2 cells.

FACS analysis of tdTomato-labeled cells revealed significantly lower percentages of IAAPs and mature AT2 cells among epithelial cells in *Fgfr2b* cKO mice (Fig. 7D) than in wild-type controls after BLM injury (Fig. 3B−D). Moreover, the IAAP and mature AT2 cell populations in *Fgfr2b* cKO mice were only marginally higher in the BLM + Met group than in the BLM group, with no significant difference (Fig. 7D and E), whereas in the *Fgfr2b* wild-type mice, the proportions of both populations were significantly higher in the BLM + Met group than in the BLM alone group (Fig. 3B−D).

These results underscore the critical role of FGFR2b signaling in both BLM injury-induced AT2 stem cell activity and Met-mediated protection against mature AT2 cell apoptosis, as well as IAAP proliferation. H&E, Masson's trichrome, and α-SMA IF staining with quantification revealed that Met treatment did not significantly attenuate BLM-induced changes in the expression of fibrotic markers or phenotypes in *Fgfr2b* cKO mice (Fig. 7F−L).

We next assessed the expression of FGF10, a high-affinity ligand for FGFR2b that is critical for AT2 cell survival and IAAP mobilization[51,53,56], in lung tissues from control, BLM, and/or Met-treated mice. Immunoblotting revealed an increase in FGF10 expression in both BLM- and Met-treated mice compared with control mice, with a slight, nonsignificant increase in the BLM + Met group compared to the BLM alone group (Supporting Information Fig. S9A and S9B). ELISA results corroborated these findings, showing a significant increase in FGF10 levels in the BLM group compared to controls, whereas only a marginal, statistically insignificant increase was observed in the Met and B + M groups compared to the BLM group (Fig. S9C). Overall, our data reveal that the Met-mediated acceleration of fibrosis resolution is closely linked to the activation of AT2 stem cells, particularly IAAPs, through a mechanism that depends on FGFR2b signaling.

3.8. Met activates the AMPK signaling pathway to upregulate Fgfr2 expression

Building on the above findings, we further investigated the mechanism by which Met regulates AT2 cells *via* FGFR2b signaling. Through KEGG pathway enrichment analysis, we found that Met treatment significantly upregulated the activity of the AMPK signaling in AT2 cells (Fig. 8A). Further validation through IF co-staining for p-AMPK and RAGE in lung tissue sections from the Ctrl, BLM, and B + M groups revealed

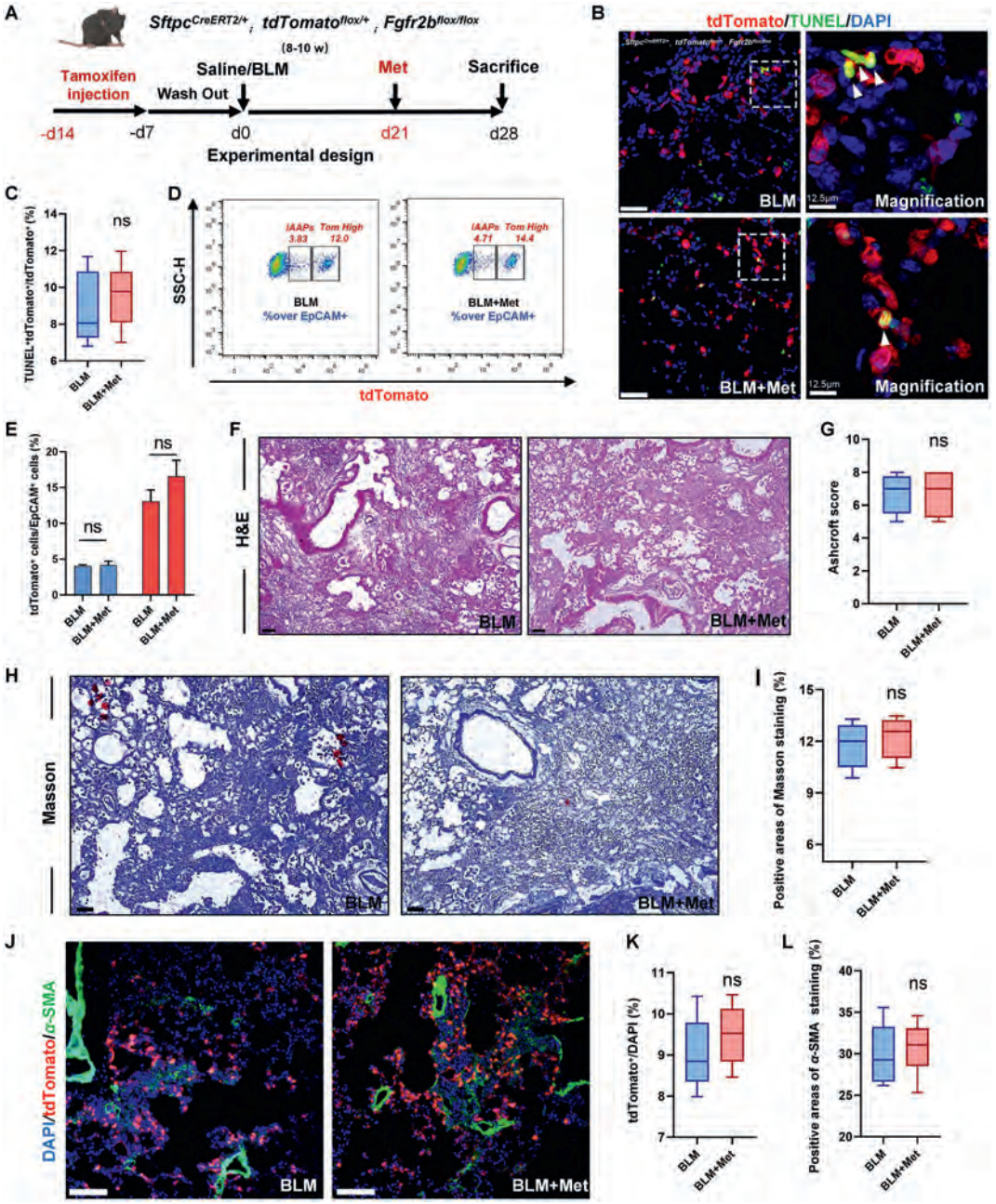

Figure 7 Met activation of AT2 stem cell activity requires FGFR2b signaling. (A) Timeline of BLM and Met treatments. (B) Immunostaining for TUNEL in the lungs of *Sftpc* lineage-traced *Fgfr2b* cKO mice in each group. Scale bar: 50 μm. (C) Quantification of the immunofluorescence data showing the percentage of TUNEL$^+$ cells among the tdTomato$^+$ cells ($n = 5$). (D) Representative flow cytometry analysis of IAAP and AT2 cells in each group. (E) Quantification of the percentage of tdTomato$^+$ cells among total EpCAM$^+$ cells (Blue: Tom^{low}; Red: Tom^{high}; $n = 3$). (F) Images of H&E-stained lungs from each group. Scale bar: 50 μm. (G) Ashcroft score determined based on H&E staining ($n = 5$). (H) Masson's trichrome staining of lung tissues from each group. Scale bar: 50 μm. (I) Statistical chart of Masson's trichrome-stained areas ($n = 5$). (J) Immunostaining for α-SMA in the lungs of *Sftpc* lineage-traced *Fgfr2b* cKO mice in each group. Scale bar: 100 μm. (K) Quantification of the immunofluorescence data showing the percentage of total tdTomato$^+$ cells among the total number of DAPI-stained cells ($n = 5$). (L) Quantification of the immunofluorescence data showing the positive area of α-SMA staining ($n = 5$). The data are presented as the mean ± SEM. ns: not significant.

that p-AMPK was localized primarily in epithelial cells with significantly increased levels in the B + M group compared with the BLM group (Fig. 8B and C). These findings indicate that Met robustly activates the AMPK pathway in AT2 cells. Furthermore, IF staining for FGFR2 revealed that the combination of BLM and Met significantly increased FGFR2 expression in AT2 cells (Fig. 8D and E). These findings suggest that Met may upregulate FGFR2 expression by activating the AMPK pathway in epithelial cells, thereby promoting BLM-induced pulmonary fibrosis.

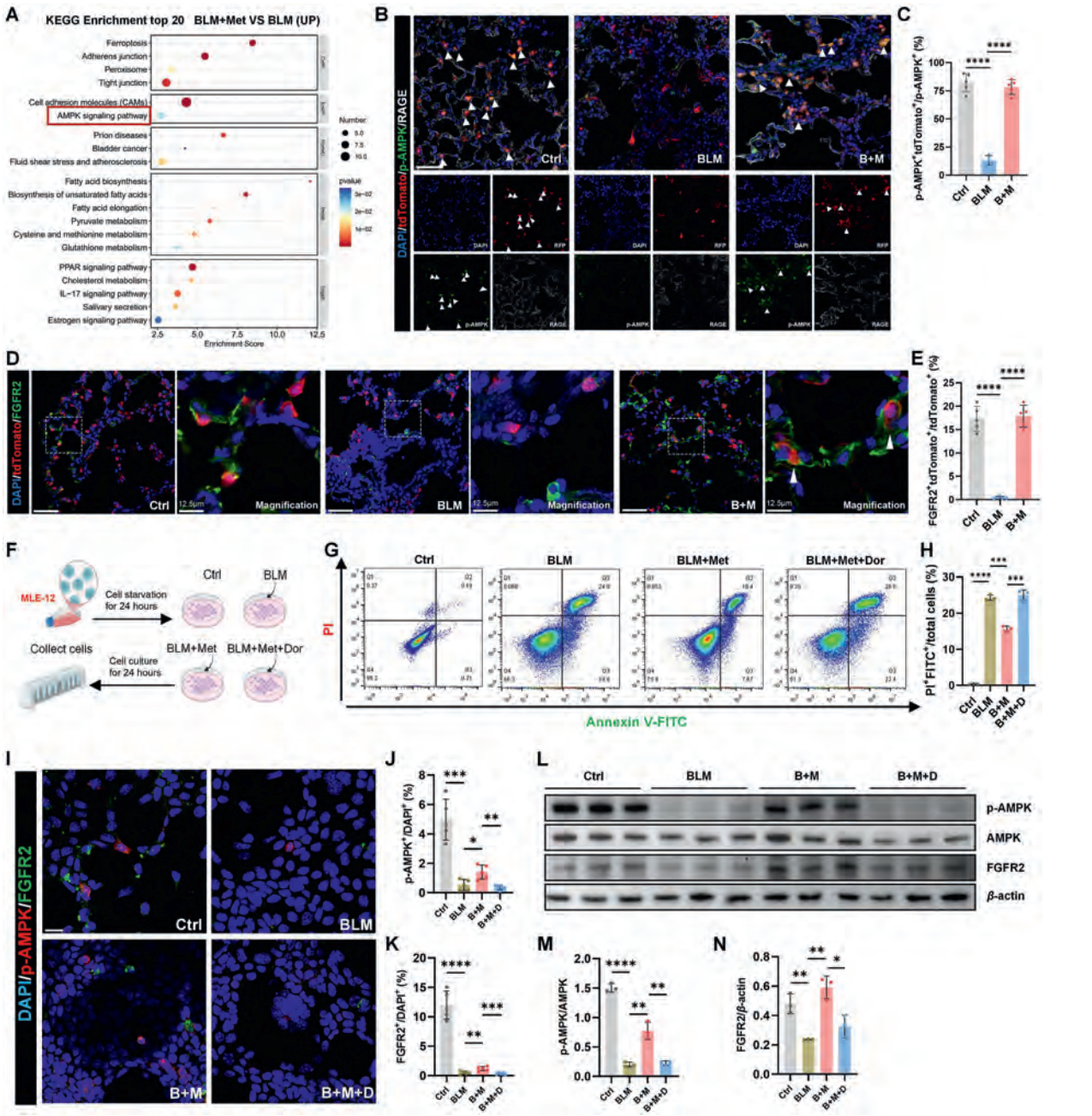

Figure 8 Met activates the AMPK signaling pathway to upregulate FGFR2 expression. (A) The KEGG pathway enrichment analysis comparing the differences between the BLM + Met and BLM groups. (B) Immunostaining for p-AMPK and RAGE in lung sections from each group. Scale bar: 50 μm. (C) Quantification of the immunofluorescence data showing the percentage of p-AMPK$^+$ tdTomato$^+$ cells among the total p-AMPK$^+$ cells ($n = 5$). (D) Immunostaining for FGFR2 in lung sections from each treatment group. Scale bar: 50 μm. (E) Quantification of the immunofluorescence data showing the percentage of FGFR2$^+$ tdTomato$^+$ cells among the total number of tdTomato$^+$ cells ($n = 5$). (F) Schematic timeline illustrating the combined treatment with BLM, Met, and dorsomorphin (D). (G) Representative FACS analysis of PI-positive cells in the control, BLM, B + M, and B + M + D treatment groups. (H) Quantification of late apoptotic (FITC$^+$/PI$^+$) cells out of total cells ($n = 3$). (I) Cellular immunofluorescence staining for p-AMPK and FGFR2. Scale bar: 20 μm. (J) Quantification of p-AMPK$^+$ cells as a percentage of the total cell population ($n = 5$). (K) Quantification of FGFR2$^+$ cells as a percentage of the total cell population ($n = 5$). (L) Relative protein expression levels were assessed by Western blotting. (M, N) Quantitative analysis of the immunoblot data ($n = 3$). The results are presented as the mean ± SEM. Statistical significance is indicated as follows: $^*P < 0.05$; $^{**}P < 0.01$; $^{***}P < 0.001$; and $^{****}P < 0.0001$.

To explore this mechanism, we used MLE-12 cells and divided them into Control, BLM, BLM + Met, and BLM + Met + Dor (dorsomorphin, an AMPK inhibitor) groups (Fig. 8F). Flow cytometry analysis was used to assess Annexin V-FITC/PI-positive cells in each group, with 0.19% double-positive cells in the control group and 24% in the BLM group. Notably, BLM + Met significantly reduced the percentage of PI-positive cells to 16.4%, whereas the addition of the AMPK inhibitor (B + M + D group) led to a pronounced increase in the percentage of double-positive cells (26%) (Fig. 8G and H).

IF co-staining for p-AMPK and FGFR2 further showed that Met treatment significantly activated the AMPK signaling pathway, leading to increased FGFR2 levels in the B + M group (Fig. 8I−K). Conversely, the AMPK pathway inhibitor markedly suppressed p-AMPK levels, resulting in a substantial decrease in FGFR2 levels in the B + M + D group (Fig. 8I−K). Immunoblotting corroborated these findings, revealing significantly decreased p-AMPK and FGFR2 levels in both the BLM and B + M + D groups compared with the controls, with a modest increase in the B + M group compared to the BLM group (Fig. 8L−N).

In summary, these data demonstrate that the activation of the AMPK pathway in epithelial cells is crucial for Met-mediated protection against apoptosis and is closely linked to increased FGFR2 expression. This pathway plays a crucial role in the protective effects of Met on fibrosis by bolstering AT2 cell survival and promoting alveolar repair through FGFR2b signaling.

4. Discussion

This study provides the first comprehensive characterization of the Met's impact on AECs. These findings reveal that Met, when administered at the peak of BLM-induced pulmonary fibrosis, significantly accelerates fibrosis resolution and promotes lung functional recovery. At the cellular level, our findings highlight that the therapeutic efficacy of Met primarily stems from its impact on AECs, with a key mechanism being the promotion of AT2 stem cell activity, thus expanding its role beyond the previously identified impact on MYFs as a target. Our data indicate that Met treatment increases AT2 cell survival and proliferation *in vivo*, with a particularly pronounced effect on the IAAP subpopulation. These findings support an important role for epithelial cell-autonomous mechanisms in Met-facilitated alveolar regeneration and fibrosis resolution.

Previous studies have shown that Met exerts antifibrotic effects by regulating metabolism, inhibiting TGFβ1, and reducing collagen synthesis, mainly through AMPK activation. Notably, evidence of AMPK-independent lipogenic differentiation in IPF lung-derived fibroblasts *in vitro via* BMP2/PPARγ activation has been reported[38]. However, paradoxically, collagen type 1 levels remain unaffected under similar conditions. In our BLM-induced injury model, Met treatment markedly upregulated *Bmp2*, *Pparg*, and *Plin2* expression while reducing α-SMA protein levels, fibrosis scores, and mature AT2 marker (*Sftpc and Etv5*) expression in BLM-injured mice. These data collectively demonstrate that Met administration at dpi21 after BLM injury, corresponding to the peak of fibrosis pathology, significantly accelerates fibrosis resolution, promoting epithelial regeneration and functional recovery.

Given that activated MYFs are primarily responsible for the secretion of matrix proteins, while newly generated LIFs support AT2 cell maintenance[44,48,49], we examined whether the Met-induced BMP2/PPARγ-driven lipogenic differentiation of MYFs contributes to alleviating the fibrosis phenotype induced by BLM. Surprisingly, inhibitors of BMP2 (Noggin) or PPARγ (oleuropein), at doses sufficient to reverse MYF to LIF differentiation, did not significantly compromise the therapeutic benefits of Met, as evidenced by stable fibrosis scores and *Col1a1* and α-SMA levels (Fig. 4). Neither inhibitor significantly affected the Met-induced expansion of mature AT2 (Tom^{High}) and IAAP (Tom^{Low}) cells nor their differentiation towards AT1 cells (Fig. 5). These findings suggest that the effects of Met on AT2 activation, particularly IAAPs, operate independently of lipogenic differentiation, supporting an epithelial cell-autonomous mechanism.

AT2 cells serve as the primary source of stem cells in the alveoli, where chronic epithelial injury and maladaptive repair are central to pulmonary fibrosis. Emerging research highlights the heterogeneity within AT2 cells, with stable and transient subpopulations contributing to lung homeostasis and regeneration[18,57−60]. Our previous work identified IAAPs as an immature AT2 subset with unique chromatin and transcriptional profiles characterized by low *Sftpc*, *Fgfr2b*, and *Etv5* levels and enriched *Pd-l1* expression. IAAPs exhibit robust expansion, survival, and differentiation potential following injury, highlighting their regenerative role[50,51].

Our current study further investigated the role of Met in mitigating apoptosis in mature AT2 cells, promoting the proliferation of AT2 cells, and enhancing their differentiation into AT1 cells (Fig. 3). Through a scRNA-seq analysis of tdTomato-labeled cells from *Sftpc* lineage-traced mice, we observed increases in the numbers of proliferating and transitioning AT2/AT1 cells, with notable IAAP enrichment, following Met treatment. The GO analysis revealed that Met mitigated the apoptosis pathway, particularly in mature AT2 cells, while increasing the number of *Rage*-positive, *Ki67*-positive cells within the tdTomato-positive population (Fig. 6E−J). These findings underscore the multifaceted role of Met in protecting AECs by reducing their apoptosis and promoting their proliferation and differentiation, which contribute to facilitating the repair of the lung epithelial structure and resolving fibrosis.

After establishing AT2 cells as significant Met targets, we investigated the molecular mechanisms regulating AT2 stem cell activity by Met. We next examined whether FGFR2b signaling underlies Met's effects in the BLM-induced fibrosis model using *Sfptc* lineage-targeted *Fgfr2b* cKO mice. The results indicated that Met's ability to increase AT2 cell survival and resolve fibrosis was largely abrogated in *Fgfr2b* deficient mice, highlighting that FGFR2b is essential for Met's effects on AT2 cells, particularly IAAPs, in accelerating fibrosis resolution. These results suggest that FGFR2b signaling is crucial for AT2 cell survival, supporting IAAP expansion and differentiation. Through KEGG pathway enrichment analysis, we found that compared to the BLM group, the BLM + Met group significantly activated the AMPK signaling pathway in AT2 cells. Our hypothesis that Met regulates FGFR2 *via* AMPK activation is supported by data showing that AMPK pathway activation occurs in epithelial cells, particularly AT2 cells, and increases with Met treatment. *In vitro* experiments with MLE-12 cells revealed that AMPK inhibition (B + M + D group) blocked AMPK activation, reduced FGFR2 levels, and significantly increased apoptosis. These findings demonstrate that AMPK activation is essential for protecting of AT2 cells from FGFR2-associated apoptosis.

Although Met targets both mesenchymal and epithelial cells, we propose that its therapeutic benefit primarily arises from epithelial cell-autonomous mechanisms, including IAAP activation and mature AT2 cell survival. Specifically, we suggest that Met alleviates AT2 cell apoptosis by activating the AMPK pathway, which stimulates IAAPs, thereby promoting their proliferation and differentiation into mature AT2/AT1 cells. IAAPs exhibit low FGFR2b and high Pd-l1 expression, whereas mature AT2 cells express high FGFR2b, but show no significant

expression of Pd-l1[50]. This may explain how AMPK activation upregulates FGFR2b expression. Notably, *Fgfr2b* knockout in *Sftpc*-lineage cells leads to apoptosis[53], and our data demonstrate that Met failed to mitigate fibrosis in *Fgfr2b* cKO mice, highlighting FGFR2b's critical role in epithelial cell repair.

Although AMPK and FGFR2 signaling pathways are functionally distinct, they may intersect through metabolic and transcriptional regulation. AMPK primarily modulates cellular metabolism, while FGFR2 governs growth and differentiation. AMPK activation influences transcription factors (*e.g.*, p53, FOXO), implicated in FGFR2-mediated processes[61−67], suggesting that AMPK may modulate FGFR2 signaling *via* metabolic reprogramming and transcriptional responses. While our data revealed close AMPK−FGFR2 association, the precise mechanisms require further investigation. Current *Sftpc*-based models lack IAAP specificity, necessitating dual recombination systems (*e.g.*, Cre and Dre recombinases) for future lineage tracing.

5. Conclusions

This study provides novel mechanistic insights into Met's effects on established fibrosis, with a focus on AECs. We demonstrate that Met accelerates fibrosis resolution *via* alveolar regeneration by activating AT2 stem cells, particularly IAAPs. While not primarily mediated by MYF-to-LIF differentiation, this process requires AMPK-FGFR2b signaling. These findings support a model wherein Met-driven activation of progenitor cells contributes to its therapeutic efficacy, advancing the mechanistic rationale for clinical translation in fibrotic lung disease.

Acknowledgments

This study was partially supported by the Discipline Cluster of Oncology of Wenzhou Medical University, China (Grant No. Z1-2023004 to Jin-San Zhang), Zhejiang Province Public Welfare Fund Project, China (Grant No. LY24H050003 to Jin-San Zhang), and the National Natural Science Foundation of China (Grant No. 82170017 to Chengshui Chen). We wish to thank Yangyang Liu from the Central Laboratory of the First Affiliated Hospital for assistance with flow cell sorting, and acknowledge the Scientific Research Center of Wenzhou Medical Univeristy for instrument access and technical consultation.

Author contributions

Yuqing Lv: Writing − original draft, Visualization, Validation, Software, Methodology, Investigation, Formal analysis, Data curation, Conceptualization. Yanxia Zhang: Investigation, Data curation, Formal analysis. Xueli Guo: Investigation, Formal analysis, Data curation. Baiqi He: Investigation, Data curation. Haibo Xu: Validation, Data curation. Ming Xu: Software, Data curation. Lihui Zou: Validation, Data curation. Handeng Lyu: Methodology, Data curation. Jin Wu: Software, Methodology, Data curation. Pingping Zeng: Investigation, Data curation. Saverio Bellusci: Writing − review & editing, Resources. Xuru Jin: Resources, Funding acquision. Chengshui Chen: Supervision, Resources, Funding acquisition. Youngchang Cho: Supervision, Resources. Xiaokun Li: Supervision, Resources, Conceptualization. Jin-San Zhang: Writing − Critical review & editing, Supervision, Resources, Funding acquisition, Conceptualization.

Conflicts of interest

The authors declare no conflicts of interest.

Appendix A. Supporting information

Supporting information to this article can be found online at https://doi.org/10.1016/j.apsb.2025.07.023.

References

1. Iommi M, Faragalli A, Bonifazi M, Mei F, Latini LL, Pompili M, et al. Prognosis and survival in idiopathic pulmonary fibrosis in the era of antifibrotic therapy in Italy: evidence from a longitudinal population study based on healthcare utilization databases. *Int J Environ Res Publ Health* 2022;**19**:16689.
2. Honda K, Saraya T, Ishii H. A real-world prognosis in idiopathic pulmonary fibrosis: a special reference to the role of antifibrotic agents for the elderly. *J Clin Med* 2023;**12**:3564.
3. Khor YH, Ng Y, Barnes H, Goh NSL, McDonald CF, Holland AE. Prognosis of idiopathic pulmonary fibrosis without anti-fibrotic therapy: a systematic review. *Eur Respir Rev* 2020;**29**:190158.
4. Renzoni E, Srihari V, Sestini P. Pathogenesis of idiopathic pulmonary fibrosis: review of recent findings. *F1000Prime Rep* 2014;**6**:69.
5. Homps-Legrand M, Crestani B, Mailleux AA. Origins of pathological myofibroblasts in lung fibrosis: insights from lineage tracing mouse models in the single-cell RNA sequencing era. *Am J Physiol Lung Cell Mol Physiol* 2023;**324**:L737−46.
6. Zabihi M, Shahriari Felordi M, Lingampally A, Bellusci S, Chu X, El Agha E. Understanding myofibroblast origin in the fibrotic lung. *Chin Med J Pulm Crit Care Med* 2024;**2**:142−50.
7. Jin T, Gao H, Wang Y, Ning Z, Bing D, Wang Y, et al. SRSF7 promotes pulmonary fibrosis through regulating PKM alternative splicing in lung fibroblasts. *Acta Pharm Sin B* 2025;**15**:3041−58.
8. Zhu W, Tan C, Zhang J. Alveolar epithelial type 2 cell dysfunction in idiopathic pulmonary fibrosis. *Lung* 2022;**200**:539−47.
9. Parimon T, Yao C, Stripp BR, Noble PW, Chen P. Alveolar epithelial type II cells as drivers of lung fibrosis in idiopathic pulmonary fibrosis. *Int J Mol Sci* 2020;**21**:2269.
10. Katzen J, Beers MF. Contributions of alveolar epithelial cell quality control to pulmonary fibrosis. *J Clin Investig* 2020;**130**:5088−99.
11. Moss BJ, Ryter SW, Rosas IO. Pathogenic mechanisms underlying idiopathic pulmonary fibrosis. *Ann Rev Pathol* 2022;**17**:515−46.
12. Lv X, Liu S, Liu C, Li Y, Zhang T, Qi J, et al. TRIB3 promotes pulmonary fibrosis through inhibiting SLUG degradation by physically interacting with MDM2. *Acta Pharm Sin B* 2023;**13**:1631−47.
13. Barkauskas CE, Cronce MJ, Rackley CR, Bowie EJ, Keene DR, Stripp BR, et al. Type 2 alveolar cells are stem cells in adult lung. *J Clin Investig* 2013;**123**:3025−36.
14. Desai TJ, Brownfield DG, Krasnow MA. Alveolar progenitor and stem cells in lung development, renewal and cancer. *Nature* 2014;**507**:190−4.
15. Liu D, Xu C, Jiang L, Zhu X. Pulmonary endogenous progenitor stem cell subpopulation: physiology, pathogenesis, and progress. *J Intensive Med* 2023;**3**:38−51.
16. Wu H, Yu Y, Huang H, Hu Y, Fu S, Wang Z, et al. Progressive pulmonary fibrosis is caused by elevated mechanical tension on alveolar stem cells. *Cell* 2020;**180**:107−21.e17.
17. Finn J, Sottoriva K, Pajcini KV, Kitajewski JK, Chen C, Zhang W, et al. Dlk1-mediated temporal regulation of Notch signaling is required for differentiation of alveolar type II to type I cells during repair. *Cell Rep* 2019;**26**:2942−54.e5.
18. Choi J, Park JE, Tsagkogeorga G, Yanagita M, Koo BK, Han N, et al. Inflammatory signals induce AT2 cell-derived damage-associated transient progenitors that mediate alveolar regeneration. *Cell Stem Cell* 2020;**27**:366−82.e7.

19. Kobayashi Y, Tata A, Konkimalla A, Katsura H, Lee RF, Ou J, et al. Persistence of a regeneration-associated, transitional alveolar epithelial cell state in pulmonary fibrosis. *Nat Cell Biol* 2020;**22**:934−46.
20. Strunz M, Simon LM, Ansari M, Kathiriya JJ, Angelidis I, Mayr CH, et al. Alveolar regeneration through a $Krt8^{+}$ transitional stem cell state that persists in human lung fibrosis. *Nat Commun* 2020;**11**:3559.
21. Adams TS, Schupp JC, Poli S, Ayaub EA, Neumark N, Ahangari F, et al. Single-cell RNA-seq reveals ectopic and aberrant lung-resident cell populations in idiopathic pulmonary fibrosis. *Sci Adv* 2020;**6**:eaba1983.
22. Auyeung VC, Downey MS, Thamsen M, Wenger TA, Backes BJ, Sheppard D, et al. IRE1α drives lung epithelial progenitor dysfunction to establish a niche for pulmonary fibrosis. *Am J Physiol Lung Cell Mol Physiol* 2022;**322**:L564−80.
23. Enomoto Y, Katsura H, Fujimura T, Ogata A, Baba S, Yamaoka A, et al. Autocrine TGF-β-positive feedback in profibrotic AT2-lineage cells plays a crucial role in non-inflammatory lung fibrogenesis. *Nat Commun* 2023;**14**:4956.
24. Ng-Blichfeldt JP, de Jong T, Kortekaas RK, Wu X, Lindner M, Guryev V, et al. TGF-β activation impairs fibroblast ability to support adult lung epithelial progenitor cell organoid formation. *Am J Physiol Lung Cell Mol Physiol* 2019;**317**:L14−28.
25. Yao C, Guan X, Carraro G, Parimon T, Liu X, Huang G, et al. Senescence of alveolar type 2 cells drives progressive pulmonary fibrosis. *Am J Respir Crit Care Med* 2021;**203**:707−17.
26. Parimon T, Chen P, Stripp BR, Liang J, Jiang D, Noble PW, et al. Senescence of alveolar epithelial progenitor cells: a critical driver of lung fibrosis. *Am J Physiol Cell Physiol* 2023;**325**:C483−95.
27. Martin-Medina A, Lehmann M, Burgy O, Hermann S, Baarsma HA, Wagner DE, et al. Increased extracellular vesicles mediate WNT5A signaling in idiopathic pulmonary fibrosis. *Am J Respir Crit Care Med* 2018;**198**:1527−38.
28. Parimon T, Yao C, Habiel DM, Ge L, Bora SA, Brauer R, et al. Syndecan-1 promotes lung fibrosis by regulating epithelial reprogramming through extracellular vesicles. *JCI Insight* 2019;**5**:e129359.
29. Wynn TA. Cellular and molecular mechanisms of fibrosis. *J Pathol* 2008;**214**:199−210.
30. García-de-Alba C, Becerril C, Ruiz V, González Y, Reyes S, García-Alvarez J, et al. Expression of matrix metalloproteases by fibrocytes: possible role in migration and homing. *Am J Respir Crit Care Med* 2010;**182**:1144−52.
31. Li Q, Park PW, Wilson CL, Parks WC. Matrilysin shedding of syndecan-1 regulates chemokine mobilization and transepithelial efflux of neutrophils in acute lung injury. *Cell* 2002;**111**:635−46.
32. Manicone AM, Huizar I, McGuire JK. Matrilysin (matrix Metalloproteinase-7) regulates anti-inflammatory and antifibrotic pulmonary dendritic cells that express CD103 ($\alpha_E\beta_7$-integrin). *Am J Pathol* 2009;**175**:2319−31.
33. McGuire JK, Li Q, Parks WC. Matrilysin (matrix metalloproteinase-7) mediates E-cadherin ectodomain shedding in injured lung epithelium. *Am J Pathol* 2003;**162**:1831−43.
34. Wang D, Deng B, Cheng L, Li J, Zhang J, Zhang X, et al. A novel and low-toxic peptide DR3penA alleviates pulmonary fibrosis by regulating the MAPK/miR-23b-5p/AQP5 signaling axis. *Acta Pharm Sin B* 2023;**13**:722−38.
35. Saito S, Alkhatib A, Kolls JK, Kondoh Y, Lasky JA. Pharmacotherapy and adjunctive treatment for idiopathic pulmonary fibrosis (IPF). *J Thorac Dis* 2019;**11**:S1740−54.
36. Park CS, Bang BR, Kwon HS, Moon KA, Kim TB, Lee KY, et al. Metformin reduces airway inflammation and remodeling *via* activation of AMP-activated protein kinase. *Biochem Pharmacol* 2012;**84**:1660−70.
37. Rangarajan S, Bone NB, Zmijewska AA, Jiang S, Park DW, Bernard K, et al. Metformin reverses established lung fibrosis in a bleomycin model. *Nat Med* 2018;**24**:1121−7.
38. Kheirollahi V, Wasnick RM, Biasin V, Vazquez-Armendariz AI, Chu X, Moiseenko A, et al. Metformin induces lipogenic differentiation in myofibroblasts to reverse lung fibrosis. *Nat Commun* 2019;**10**:2987.
39. Xiao H, Huang X, Wang S, Liu Z, Dong R, Song D, et al. Metformin ameliorates bleomycin-induced pulmonary fibrosis in mice by suppressing IGF-1. *Am J Transl Res* 2020;**12**:940−9.
40. Ji H, Dong H, Lan Y, Bi Y, Gu X, Han Y, et al. Metformin attenuates fibroblast activation during pulmonary fibrosis by targeting S100A4 *via* AMPK−STAT3 axis. *Front Pharmacol* 2023;**14**:1089812.
41. Gu X, Han YY, Yang CY, Ji HM, Lan YJ, Bi YQ, et al. Activated AMPK by metformin protects against fibroblast proliferation during pulmonary fibrosis by suppressing FOXM1. *Pharmacol Res* 2021;**173**:105844.
42. Quan MY, Yan X, Miao W, Li X, Li J, Yang L, et al. Metformin alleviates benzo[*a*]pyrene-induced alveolar injury by inhibiting necroptosis and protecting AT2 cells. *Ecotoxicol Environ Saf* 2024;**272**:116094.
43. Vaccaro C, Brody JS. Ultrastructure of developing alveoli. I. The role of the interstitial fibroblast. *Anat Rec* 1978;**192**:467−79.
44. McGowan SE, Torday JS. The pulmonary lipofibroblast (lipid interstitial cell) and its contributions to alveolar development. *Annu Rev Physiol* 1997;**59**:43−62.
45. O'Hare KH, Sheridan MN. Electron microscopic observations on the morphogenesis of the albino rat lung, with special reference to pulmonary epithelial cells. *Am J Anat* 1970;**127**:181−205.
46. El Agha E, Thannickal VJ. The lung mesenchyme in development, regeneration, and fibrosis. *J Clin Investig* 2023;**133**:e170498.
47. Liberti DC, Kremp MM, Liberti 3rd WA, Penkala IJ, Li S, Zhou S, et al. Alveolar epithelial cell fate is maintained in a spatially restricted manner to promote lung regeneration after acute injury. *Cell Rep* 2021;**35**:109092.
48. Lv YQ, Dhlamini Q, Chen C, Li X, Bellusci S, Zhang JS. FGF10 and lipofibroblasts in lung homeostasis and disease: insights gained from the adipocytes. *Front Cell Dev Biol* 2021;**9**:645400.
49. Taghizadeh S, Heiner M, Vazquez-Armendariz AI, Wilhelm J, Herold S, Chen C, et al. Characterization in mice of the resident mesenchymal niche maintaining AT2 stem cell proliferation in homeostasis and disease. *Stem Cell* 2021;**39**:1382−94.
50. Ahmadvand N, Khosravi F, Lingampally A, Wasnick R, Vazquez-Armendariz AI, Carraro G, et al. Identification of a novel subset of alveolar type 2 cells enriched in PD-L1 and expanded following pneumonectomy. *Eur Respir J* 2021;**58**:2004168.
51. Lv YQ, Cai GF, Zeng PP, Dhlamini Q, Chen LF, Chen JJ, et al. FGF10 therapeutic administration promotes mobilization of injury-activated alveolar progenitors in a mouse fibrosis model. *Cells* 2022;**11**:2396.
52. Ahmadvand N, Carraro G, Jones MR, Shalashova I, Noori A, Wilhelm J, et al. Cell-surface programmed death ligand-1 expression identifies a sub-population of distal epithelial cells enriched in idiopathic pulmonary fibrosis. *Cells* 2022;**11**:1593.
53. Ahmadvand N, Lingampally A, Khosravi F, Vazquez-Armendariz AI, Rivetti S, Jones MR, et al. Fgfr2b signaling is essential for the maintenance of the alveolar epithelial type 2 lineage during lung homeostasis in mice. *Cell Mol Life Sci* 2022;**79**:302.
54. De Moerlooze L, Spencer-Dene B, Revest JM, Hajihosseini M, Rosewell I, Dickson C. An important role for the IIIb isoform of fibroblast growth factor receptor 2 (FGFR2) in mesenchymal−epithelial signalling during mouse organogenesis. *Development* 2000;**127**:483−92.
55. Chong L, Ahmadvand N, Noori A, Lv Y, Chen C, Bellusci S, et al. Injury activated alveolar progenitors (IAAPs): the underdog of lung repair. *Cell Mol Life Sci* 2023;**80**:145.
56. Jones MR, Lingampally A, Ahmadvand N, Chong L, Wu J, Wilhem J, et al. FGFR2b signalling restricts lineage-flexible alveolar progenitors during mouse lung development and converges in mature alveolar type 2 cells. *Cell Mol Life Sci* 2022;**79**:609.
57. Chen Q, Liu Y. Heterogeneous groups of alveolar type II cells in lung homeostasis and repair. *Am J Physiol Cell Physiol* 2020;**319**:C991−6.
58. Zacharias WJ, Frank DB, Zepp JA, Morley MP, Alkhaleel FA, Kong J, et al. Regeneration of the lung alveolus by an evolutionarily conserved epithelial progenitor. *Nature* 2018;**555**:251−5.

59. Nabhan AN, Brownfield DG, Harbury PB, Krasnow MA, Desai TJ. Single-cell Wnt signaling niches maintain stemness of alveolar type 2 cells. *Science* 2018;**359**:1118−23.
60. Kadur Lakshminarasimha Murthy P, Sontake V, Tata A, Kobayashi Y, Macadlo L, Okuda K, et al. Human distal lung maps and lineage hierarchies reveal a bipotent progenitor. *Nature* 2022;**604**:111−9.
61. Hardie DG. AMP-activated protein kinase: an energy sensor that regulates all aspects of cell function. *Genes Dev* 2011;**25**:1895−908.
62. Chen K, Rao Z, Dong S, Chen Y, Wang X, Luo Y, et al. Roles of the fibroblast growth factor signal transduction system in tissue injury repair. *Burns Trauma* 2022;**10**:tkac005.
63. Nakashima K, Yakabe Y. AMPK activation stimulates myofibrillar protein degradation and expression of atrophy-related ubiquitin ligases by increasing FOXO transcription factors in C2C12 myotubes. *Biosci Biotechnol Biochem* 2007;**71**:1650−6.
64. Greer EL, Oskoui PR, Banko MR, Maniar JM, Gygi MP, Gygi SP, et al. The energy sensor AMP-activated protein kinase directly regulates the mammalian FOXO3 transcription factor. *J Biol Chem* 2007; **282**:30107−19.
65. Jones RG, Plas DR, Kubek S, Buzzai M, Mu J, Xu Y, et al. AMP-activated protein kinase induces a p53-dependent metabolic checkpoint. *Mol Cell* 2005;**18**:283−93.
66. Nieminen AI, Eskelinen VM, Haikala HM, Tervonen TA, Yan Y, Partanen JI, et al. Myc-induced AMPK-phospho p53 pathway activates Bak to sensitize mitochondrial apoptosis. *Proc Natl Acad Sci U S A* 2013;**110**:E1839−48.
67. Sluzalska KD, Slawski J, Sochacka M, Lampart A, Otlewski J, Zakrzewska M. Intracellular partners of fibroblast growth factors 1 and 2—implications for functions. *Cytokine Growth Factor Rev* 2021;**57**: 93−111.